A non-linear Ritz method for progressive failure analysis of variable angle tow composite laminates

Article *in* Mechanics of Advanced Materials and Structures · October 2022

DOI: 10.1080/15376494.2022.2134951

4 authors:

Dario Campagna
Università degli Studi di Palermo
7 PUBLICATIONS **6** CITATIONS
SEE PROFILE

Alberto Milazzo
Università degli Studi di Palermo
176 PUBLICATIONS **2,102** CITATIONS
SEE PROFILE

Ivano Benedetti
Università degli Studi di Palermo
143 PUBLICATIONS **1,668** CITATIONS
SEE PROFILE

Vincenzo Oliveri
University of Limerick
52 PUBLICATIONS **609** CITATIONS
SEE PROFILE

A non-linear Ritz method for progressive failure analysis of variable angle tow composite laminates

D. Campagna[1], A. Milazzo[1], I. Benedetti[1,*] and V. Oliveri[2]

[1] *Department of Engineering, University of Palermo, Viale delle Scienze, Edificio 8, 90128, Palermo, Italy.*

[2] *School of Engineering and Bernal Institute, University of Limerick, V94 T9PX, Limerick, Ireland.*

[*] *Corresponding author: ivano.benedetti@unipa.it*

Abstract

A Ritz formulation for non-linear analysis of damage initiation and evolution in variable angle tow composite plates under progressive loading is presented. The model is built on a few key items. It assumes first order shear deformation theory kinematics and non-liner strains in the von Kármán sense. The constitutive relationships are formulated in the framework of continuum damage mechanics at the ply level, so that each laminate layer can experience in-plane damage initiation and evolution, then reflected in material softening and loss of local stiffness. A Ritz polynomial expansion of the primary variables and the minimization of the total potential energy provide the discrete solution equations, which are then solved with an incremental-iterative approach for capturing damage evolution. A few tests have been successfully performed to validate the approach. Eventually, some original results about variable angle tow plates under progressive in-plane compression loads highlight the effect of damage on the post-buckling response.

Keywords — Continuum Damage Mechanics, Failure analysis, Variable angle tow composites, Ritz method, Non-linear analysis

1 Introduction

Thanks to their properties, namely low density, high stiffness and strength, low fatigue susceptibility, multilayered composite materials are used in a variety of engineering fields, including aerospace, naval and automotive, where lightweight structural components are particularly valuable [1]. Recently, the development of new manufacturing techniques, such as automated fibre placement, automated tape laying, and additive manufacturing [2–5], has promoted the design of composite structures with variable mechanical properties, allowing the realization of variable angle tow (VAT) laminates, which are obtained by varying the fibre orientation as a function of the position considered over the structure [6,7]. The advantages offered by such class of laminates are nowadays well-known and have been extensively studied [8–10].

Besides developing new manufacturing techniques for the production of advanced materials and structural components, designers and engineers need modelling and computational tools able to predict, with reasonable accuracy, the structural response of the designed components. Such demand becomes particularly relevant if the width of the materials design space, allowed by the novel manufacturing techniques, is considered. In such a context, where several process and material parameters have huge influence on the quality of the artifacts, the availability of effective computational tools may help reduce the costs of experimental campaigns needed for the development of new material configurations, thus contributing to unleashing the higher potential of new manufacturing/materials routes.

The Finite Element Method (FEM), which has also reached a well-established commercial maturity, is one of the most popular computational approaches to structural problems [11, 12]. The accuracy of FEM is closely related to the quality of the employed mesh that, in the case of VAT laminates, typically requires a high number of elements, due to the variation of the in-plane and through-the-thickness material properties, thus leading to high computational costs [13, 14]. Different mesh-less techniques have been proposed as alternatives to FEM to address such issues and possibly speed up the analysis while maintaining a high level of accuracy, see e.g. Ref. [15]; in this context, the Ritz method, which may be seen as a global mesh-less technique, has proven effective for the analysis of classical, laminated and VAT composite structures [16–21].

To fully exploit the benefits of VAT composites and identify their operational domain, it is necessary to assess and possibly predict the onset and evolution of damage, as done for

other engineering materials and traditional straight-fibre laminates. Different approaches have been used in the literature to model the initiation and evolution of damage in composite structures; depending on the scale of the idealization, from micro- through meso- to macro-scale, damage can be modelled using different techniques.

Micromechanical approaches are commonly used at the micro-scale, where the evolution of damage is represented either as matrix softening or fibre breaking, with both the matrix and the fibres explicitly represented in the so-called Representative Volume Element (RVE) [22–25]. Such methods are often employed to investigate basic damage initiation mechanisms and the material response before cracks or delaminations localize at the ply or laminate scale. At the opposite macro-scale or component level, a hard discontinuity, such as a crack or concentrated loss of material stiffness, is frequently used to describe damage and its influence on the structural functionality or safety [18, 26, 27].

On the other hand, in meso-scale models, where each ply is represented as orthotropic and homogeneous, different modelling strategies have been proposed to model damage processes; one of the most established is Continuum Damage Mechanics (CDM), see e.g. Refs. [28, 29], where damage is represented as a progressive loss of material stiffness. CDM is today widely employed and it has been successfully used for the analysis of a large variety of materials, in nano-mechanics investigations [30] and in in multi-scale applications [31].

The initiation and evolution of damage in composites has been investigated employing CDM in the framework of FEM by several authors. As an example, Maimí et al. [32, 33] developed a CDM-FE model with damage activation functions based on $LaRC04$ failure criteria for the prediction of the onset and evolution of intra-laminar failure mechanisms; Ferreira et al. [34] developed a higher-order FE model that models progressive damage using generalised kinematics; Lopes and coworkers [35] implemented a user-developed continuum damage model in the commercial FE software `ABAQUS` to investigate progressive damage evolution in VAT composite laminates in post-buckling, up to and structural failure due to fibre and matrix damage accumulation. Finite elements formulations have also been employed to develop three dimensional CDM-based material models to simulate the progressive intra-laminar degradation of fiber reinforced laminates as well as delamination using cohesive interfaces between layers [36–38].

On the other hand, very few studies have dealt with the development of Ritz approaches for the analysis of progressive damage in straight-fibre composite laminates. Yang and Hayman used an instantaneous and a linear degradation model to develop a semi-analytical

method for estimating the ultimate strength of rectangular composite laminates subjected to uniaxial in-plane compression [39, 40]. To the best of the authors' knowledge, no Ritz approach has been developed for the study of progressive damage in VAT composites, which is the main aim of the present work.

The manuscript is structured as follows: Section 2 specifies the considered problem, introduces the geometric description of the plate, the kinematic model and the constitutive relations employed to take into account the presence of damage; next, the governing equations are derived using the Ritz approximation and the principle of minimum potential energy, which are written in incremental form in order to solve the non-linear damage evolution problem. In Section 3 the proposed method is first validated for both small and moderately-large strains and then used for the analysis of different VAT laminates, to show its potential. Section 4 discusses strengths and limitations of the present work, before *Conclusions* are drawn.

2 Mechanical formulation

In this section the key items of the formulation are briefly presented and discussed. After identifying the class of mechanical problems considered in the study, the details about the kinematic and constitutive assumptions are presented. The weak formulation of the problem, governing the equilibrium at each load step, the features of the Ritz approximation and the solution incremental-iterative scheme are then discussed, before applying the method to some test applications.

2.1 Problem definition

Consider a quadrilateral composite plate, whose geometry is schematically represented in Fig.(1), referred to a Cartesian coordinates system identified by the axis x_3, directed along the plate thickness, and the axes x_1 and x_2, spanning the reference mid-plane of the plate. The 2D domain occupied by the plate over the reference mid-plane is denoted by Ω, while $\partial\Omega$ identifies its boundary; the plate thickness is denoted by h and each composite lamina is located between $x_3 = h_{k-1}$ and $x_3 = h_k$, with k denoting the lamina considered, so the bottom and top surfaces are identified by $x_3 = -h/2$ and $x_3 = h/2$ respectively.

In order to model general quadrilateral plates, a natural coordinate system $(\xi, \eta) \in$

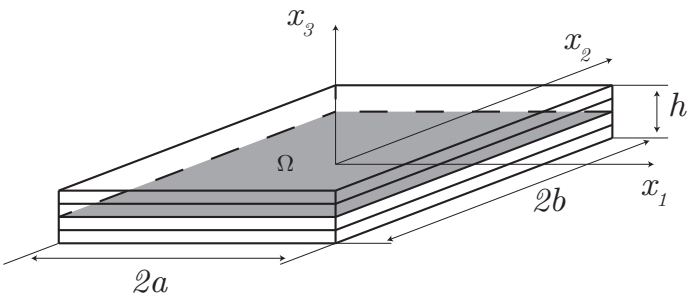

Figure 1: Schematic representation of the VAT composite plate.

$[-1,1] \times [-1,1]$, mapping the plate mid-plane into a square domain, is introduced, see Fig.(2), so that the in-plane coordinates are given by

$$x_i = \sum_{\alpha=1}^{4} g_\alpha(\xi,\eta) x_{i\alpha}, \qquad i = 1,2 \tag{1}$$

where $x_{i\alpha}$ are the coordinates of the α-*th* vertex of the plate mid-plane and g_α are the standard bi-linear shape functions, namely,

$$g_\alpha = \frac{(-1)^{\alpha-1}}{4}(\xi+\xi_\alpha)(\eta+\eta_\alpha), \qquad \alpha = 1,\dots,4 \tag{2}$$

where $(\xi_\alpha, \eta_\alpha)$ are the natural coordinates of the four vertices of the square mapping the plate mid-plane.

2.2 Plate Kinematics and strain-displacement relationship

Adopting the First order Shear Deformation Theory (FSDT), the displacements $\boldsymbol{d} = \{d_1, d_2, d_3\}^\intercal$ of the points of the plate in the reference system are given by

$$\boldsymbol{d} = \boldsymbol{u} + x_3 \boldsymbol{L}\boldsymbol{\vartheta} + \overline{\boldsymbol{w}}, \qquad \boldsymbol{L} = \begin{bmatrix} 1 & 0 & 0 \\ 0 & 1 & 0 \end{bmatrix}^\intercal \tag{3}$$

where $\boldsymbol{u} = \{u_1, u_2, u_3\}^\intercal$ and $\boldsymbol{\vartheta} = \{\vartheta_1, \vartheta_2\}^\intercal$ collect the reference plane displacement components and the section rotations, respectively, and $\overline{\boldsymbol{w}} = \{0, 0, \overline{w}\}^\intercal$ collects the components of prescribed initial displacements, which may describe the possible presence of geometrical

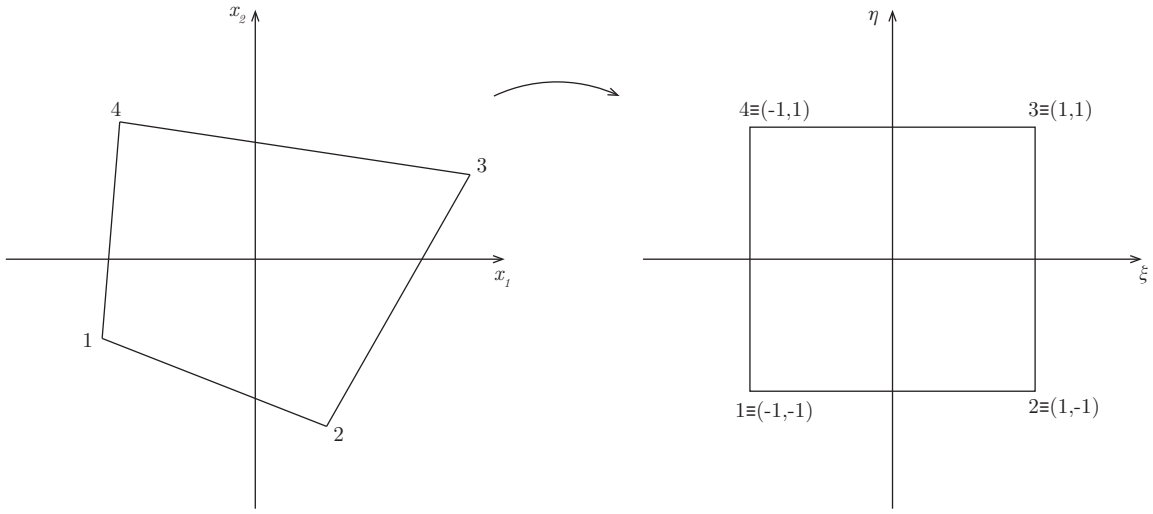

Figure 2: Plate mid-plane mapping.

plate imperfections.

The strains components may be collected in the vector

$$\boldsymbol{e} = \{e_{11}, e_{22}, e_{12}, e_{13}, e_{23}, e_{33}\}^{\intercal} = \left\{ \begin{array}{c} \boldsymbol{e}_p \\ \boldsymbol{e}_n \end{array} \right\}, \tag{4}$$

where $\boldsymbol{e}_p = \{e_{11}, e_{22}, e_{12}\}^{\intercal}$ and $\boldsymbol{e}_n = \{e_{13}, e_{23}, e_{33}\}^{\intercal}$ collect the in-plane and out-of-plane components of strains respectively.

Admitting geometric non-linearity in the von Kármán sense, the strain-displacement relationships may be written as

$$\begin{aligned} \boldsymbol{e}_p = \boldsymbol{\mathcal{D}}_p \boldsymbol{u} + \frac{1}{2} \left(\boldsymbol{\mathcal{D}}_p \otimes u_3\right) \boldsymbol{\mathcal{D}}_n \boldsymbol{u} + x_3 \boldsymbol{\mathcal{D}}_p \boldsymbol{L} \boldsymbol{\vartheta} + \left(\boldsymbol{\mathcal{D}}_p \otimes \overline{w}\right) \boldsymbol{\mathcal{D}}_n \boldsymbol{u} = \\ = \boldsymbol{\varepsilon}_p + \boldsymbol{\varepsilon}_{nl} + x_3 \boldsymbol{\kappa} + \bar{\boldsymbol{\varepsilon}} = \\ = \boldsymbol{\varepsilon} + x_3 \boldsymbol{\kappa} \end{aligned} \tag{5}$$

and

$$\boldsymbol{e}_n = \boldsymbol{\mathcal{D}}_n \boldsymbol{u} + \boldsymbol{L} \boldsymbol{\vartheta} = \boldsymbol{\gamma} \tag{6}$$

where $\boldsymbol{\mathcal{D}}_p$ and $\boldsymbol{\mathcal{D}}_n$ are matrix linear differential operators defined as

$$\boldsymbol{\mathcal{D}}_p = \begin{bmatrix} \partial_{x_1} & 0 & 0 \\ 0 & \partial_{x_2} & 0 \\ \partial_{x_2} & \partial_{x_1} & 0 \end{bmatrix} \qquad \boldsymbol{\mathcal{D}}_n = \begin{bmatrix} 0 & 0 & \partial_{x_1} \\ 0 & 0 & \partial_{x_2} \\ 0 & 0 & 0 \end{bmatrix} \tag{7}$$

with $\partial_{x_i} = \partial(\circ)/\partial x_i$. In Eqs.(5-6), the symbol $\otimes$ denotes the Kronecker product, while $\boldsymbol{\varepsilon}$, $\boldsymbol{\kappa}$ and $\boldsymbol{\gamma}$ denote the in-plane strains, curvatures and shear strains vectors, respectively; the subscript nl denotes non-linear terms induced by the von Kármán assumption.

2.3 Plate constitutive relations in presence of damage

In this section, the constitutive relations for VAT laminae are presented considering the possible presence of damage. Using the damage model developed by Matzenmiller et al. [28], the material stiffness coefficients are degraded by means of four damage indices, two associated with either tensile or compression loading along the fiber direction, namely ω_{ft} and ω_{fc} and two associated with either tensile or compression loading along the direction transversal to the fibers, i.e. ω_{mt} and ω_{mc}. On the other hand, it is worth underlining that the constitutive relations are written in the local material coordinate system and are a function of the in-plane coordinates, due to the variation of the in-plane fiber orientation $\theta(x_1, x_2)$ for a VAT lamina. This dependency is omitted in the subsequent equations for the sake of readability.

In the framework of CDM, employing the damage indices ω introduced above, one can obtain the relation between nominal in plane stress components, collected in $\tilde{\boldsymbol{\sigma}}_p$, and the effective stress components, collected in $\hat{\boldsymbol{\sigma}}_p$, as

$$\hat{\boldsymbol{\sigma}}_p = \boldsymbol{M}\tilde{\boldsymbol{\sigma}}_p, \tag{8}$$

where $\boldsymbol{M}$ is a damage operator defined as

$$\boldsymbol{M} = \begin{bmatrix} \frac{1}{1-\omega_1} & 0 & 0 \\ 0 & \frac{1}{1-\omega_2} & 0 \\ 0 & 0 & \frac{1}{1-\omega_6} \end{bmatrix}, \tag{9}$$

with ω_1, ω_2 and ω_6 being the longitudinal (fiber–dominated), transverse (matrix–dominated)

and shear damage indices respectively, defined as

$$\omega_1 = \begin{cases} \omega_{ft} & \text{if} \quad \hat{\sigma}_{11} \geq 0 \\ \omega_{fc} & \text{if} \quad \hat{\sigma}_{11} < 0 \end{cases} \qquad \omega_2 = \begin{cases} \omega_{mt} & \text{if} \quad \hat{\sigma}_{22} \geq 0 \\ \omega_{mc} & \text{if} \quad \hat{\sigma}_{22} < 0 \end{cases} \tag{10}$$

and

$$\omega_6 = 1 - (1 - \omega_{ft})(1 - \omega_{fc})(1 - \omega_{mt})(1 - \omega_{mc}), \tag{11}$$

Each damage index ω_i can vary between 0, when no damage is present, and 1, when material failure takes place.

Using the definition in Eq.(8) with the stress-strain relations gives

$$\tilde{\boldsymbol{e}}_p = \boldsymbol{S}\hat{\boldsymbol{\sigma}}_p = \boldsymbol{S}\boldsymbol{M}\tilde{\boldsymbol{\sigma}}_p \tag{12}$$

where $\tilde{\boldsymbol{e}}_p$ collects the in-plane strain in the local material coordinate system and

$$\boldsymbol{S} = \begin{bmatrix} \frac{1}{E_1} & -\frac{\nu_{21}}{E_1} & 0 \\ -\frac{\nu_{12}}{E_2} & \frac{1}{E_2} & 0 \\ 0 & 0 & \frac{1}{G_{12}} \end{bmatrix} \tag{13}$$

is the compliance matrix, E_i is the Young's modulus, ν_{ij} are the Poisson's coefficients and G_{12} is the shear modulus. Defining the damage compliance tensor as

$$\hat{\boldsymbol{S}} = \boldsymbol{S}\boldsymbol{M} = \begin{bmatrix} \frac{1}{E_1(1-\omega_1)} & -\frac{\nu_{21}}{E_1} & 0 \\ -\frac{\nu_{12}}{E_2} & \frac{1}{E_2(1-\omega_2)} & 0 \\ 0 & 0 & \frac{1}{G_{12}(1-\omega_6)} \end{bmatrix}, \tag{14}$$

where the assumptions on the degradation of the Poisson ratio made by Matzenmiller et al. [28] have been adopted, and substituting in Eq.(12), one obtains the following constitutive relation

$$\tilde{\boldsymbol{\sigma}}_p = \hat{\boldsymbol{S}}^{-1}\tilde{\boldsymbol{e}}_p = \hat{\boldsymbol{C}}\tilde{\boldsymbol{e}}_p, \tag{15}$$

where $\hat{\boldsymbol{C}}$ is the stiffness matrix in presence of damage, explicitly given by

$$\hat{\boldsymbol{C}} = \frac{1}{D}\begin{bmatrix} (1-\omega_1)E_1 & (1-\omega_1)(1-\omega_2)\nu_{21}E_1 & 0 \\ (1-\omega_1)(1-\omega_2)\nu_{12}E_2 & (1-\omega_2)E_2 & 0 \\ 0 & 0 & D(1-\omega_6)G_{12} \end{bmatrix}, \tag{16}$$

with

$$D = 1-(1-\omega_1)(1-\omega_2)\nu_{12}\nu_{21}. \tag{17}$$

The plate constitutive equations may be obtained following the classical procedure given in Ref. [41] and read as

$$\begin{Bmatrix} \boldsymbol{N} \\ \boldsymbol{M} \\ \boldsymbol{T} \end{Bmatrix} = \begin{bmatrix} \boldsymbol{A} & \boldsymbol{B} & 0 \\ \boldsymbol{B} & \boldsymbol{D} & 0 \\ 0 & 0 & \boldsymbol{A}_s \end{bmatrix} \begin{Bmatrix} \boldsymbol{\varepsilon} \\ \boldsymbol{\kappa} \\ \boldsymbol{\gamma} \end{Bmatrix}, \tag{18}$$

where the membrane stress $\boldsymbol{N} = \{N_{11}, N_{22}, N_{12}\}^\intercal$, the moments per unit length $\boldsymbol{M} = \{M_{11}, M_{22}, M_{12}\}^\intercal$ and the transverse stress resultants $\boldsymbol{T} = \{T_{13}, T_{23}\}^\intercal$ are given by

$$\boldsymbol{N} = \int_{-h/2}^{h/2} \boldsymbol{\sigma}_p \, dx_3, \qquad \boldsymbol{M} = \int_{-h/2}^{h/2} \boldsymbol{\sigma}_p x_3 \, dx_3, \qquad \boldsymbol{T} = \int_{-h/2}^{h/2} K_s \boldsymbol{\sigma}_n \, dx_3, \tag{19}$$

where K_s is a shear correction factor, while the generalized stiffness matrices are

$$\begin{aligned} \boldsymbol{A} &= \sum_{k=1}^{N_{ply}} \int_{h_{k-1}}^{h_k} \boldsymbol{Q}_p^{\langle k \rangle}(\theta) \, dx_3 & \boldsymbol{B} &= \sum_{k=1}^{N_{ply}} \int_{h_{k-1}}^{h_k} x_3 \, \boldsymbol{Q}_p^{\langle k \rangle}(\theta) \, dx_3 \\ \boldsymbol{D} &= \sum_{k=1}^{N_{ply}} \int_{h_{k-1}}^{h_k} x_3^2 \, \boldsymbol{Q}_p^{\langle k \rangle}(\theta) \, dx_3 & \boldsymbol{A}_s &= \sum_{k=1}^{N_{ply}} \int_{h_{k-1}}^{h_k} \boldsymbol{Q}_n^{\langle k \rangle}(\theta) \, dx_3, \end{aligned} \tag{20}$$

where, for each *k-th* ply, $\boldsymbol{Q}_p^{\langle k \rangle}(\theta) = \boldsymbol{L}_p(\theta) \, \hat{\boldsymbol{C}}^{\langle k \rangle} \boldsymbol{L}_p^\intercal(\theta)$ and $\boldsymbol{Q}_n^{\langle k \rangle}(\theta) = \boldsymbol{L}_n(\theta) \, \hat{\boldsymbol{C}}_n^{\langle k \rangle} \boldsymbol{L}_n^\intercal(\theta)$ contain ply stiffness coefficients that depend on the fiber orientation $\theta(x_1, x_2)$; the matrix $\hat{\boldsymbol{C}}^{\langle k \rangle}$ is defined in Eq.(16) and depends on the local damage level, the rotation matrices $\boldsymbol{L}_p$ and $\boldsymbol{L}_n$ contain the direction cosines and depend on the local fiber orientation $\theta(x_1, x_2)$ and

the matrix $\boldsymbol{C}_n$ is given by

$$\boldsymbol{C}_n = \begin{bmatrix} G_{23} & 0 \\ 0 & G_{13} \end{bmatrix}. \tag{21}$$

2.3.1 Damage onset and evolution

In the present work, the damage analysis is based on a material degradation model. After an activation threshold is overcome, the corresponding damage index starts evolving according to an evolution law, thus inducing strain softening in the constitutive material response.

Damage onset is tracked in the framework of Hashin's theory [42, 43], which considers four different activation criteria along the fibers and matrix-dominated transverse directions under either tensile or compression loading. They are defined as follows.

Fiber tension:

$$F_{ft} = \left(\frac{\hat{\sigma}_{11}}{X_T}\right)^2 = 1 \tag{22a}$$

Fiber compression:

$$F_{fc} = \left(\frac{\hat{\sigma}_{11}}{X_C}\right)^2 = 1 \tag{22b}$$

Matrix tension:

$$F_{mt} = \left(\frac{\hat{\sigma}_{22}}{Y_T}\right)^2 + \left(\frac{\hat{\sigma}_{12}}{S_L}\right)^2 = 1 \tag{22c}$$

Matrix compression:

$$F_{mc} = \left(\frac{\hat{\sigma}_{22}}{2S_L}\right)^2 + \left[\left(\frac{Y_C}{2S_T}\right)^2 - 1\right]\frac{\hat{\sigma}_{22}}{Y_C} + \left(\frac{\hat{\sigma}_{12}}{S_L}\right)^2 = 1 \tag{22d}$$

In Eqs.(22), $\hat{\sigma}_{ij}$ are the components of the stress tensor computed from Eq.(8) and X_T, X_C , Y_T ,Y_C, S_L, S_T are the ply strengths associated with each loading mode and direction. The shear transverse strength S_T, if is not available, can be computed as $S_T = 0.5Y_C$ [42].

Following the onset of damage, further increases of the effective loads generally result in the evolution of the activated damage indices and thus in the the degradation of the material properties associated with them. Referring to a linear softening law, as schematically shown in Fig.(3), upon defining the following *equivalent strains* for each loading/damage mode

$$\textit{Fibers} \quad \begin{cases} e_{ft,eq} = \langle e_{11} \rangle \\ e_{fc,eq} = \langle -e_{11} \rangle \end{cases} \qquad \textit{Matrix} \quad \begin{cases} e_{mt,eq} = \sqrt{\langle e_{22} \rangle^2 + e_{12}^2} \\ e_{mc,eq} = \sqrt{\langle -e_{22} \rangle^2 + e_{12}^2} \end{cases} \tag{23}$$

where $\langle\circ\rangle = (\circ + |\circ|)/2$ denotes the Macaulay brackets, the current value of the *i-th* damage index can be computed considering the evolution, during the loading process, of the quantities

$$\omega_i(\tau) = \frac{e^f_{i,eq}\left(e_{i,eq} - e^0_{i,eq}\right)}{e_{i,eq}\left(e^f_{i,eq} - e^0_{i,eq}\right)}, \qquad i = ft, fc, mt, mc, \tag{24}$$

where τ denotes a generic loading/time ordering parameter spanning the loading history $\mathscr{H}$, $e^0_{i,eq}$ is the equivalent strain at the onset of damage and $e^f_{i,eq} = \alpha_i\, e^0_{i,eq}$ is the equivalent strain at rupture; in particular, to ensure a monotonically increasing evolution, the current value of the *i-th* damage index is defined as

$$\omega_i = \max\{0, \max_{\tau\in\mathscr{H}}\{\omega_i(\tau)\}\}. \tag{25}$$

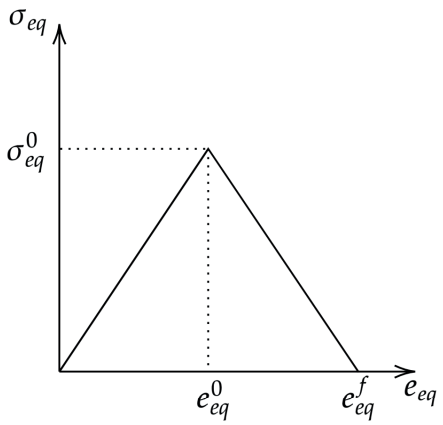

Figure 3: Adopted stress-strain softening curve.

The area under the stress-strain curve in Fig.(3) corresponds to the energy dissipated per unit volume $g = \int_0^{e^f_{eq}} \sigma_{eq} de_{eq}$ in the loading process until failure. Typically, in FE damage models, the strain softening behavior is expressed in terms of equivalent stresses VS equivalent displacements, which are used to define the energy dissipated per unit area, namely the fracture energy $G = \int_0^{\delta^f_{eq}} \sigma_{eq} d\delta_{eq}$. The latter definition allows the use of the fracture energy as input material parameter to compute the final equivalent displacement. Alternatively, as proposed in Refs. [39, 44] and adopted in the present work, it is possible to provide the equivalent strain ratio α as an input parameter.

2.4 Problem discretization and incremental solution

Considering the non-linear evolution of damage under progressive loading, the solution of the considered mechanical problem requires the implementation of an incremental-iterative approach, which will be described in this section. The discrete governing equations at a given load step can however be obtained stating the stationarity of the plate total potential energy and employing the plate kinematics assumptions, the constitutive equations and the Ritz approximation of the kinematic primary variables. Once the discrete equations are available, the adoption of a suitable incremental-iterative scheme allows capturing the evolving damage and the associated variation of the structure stiffness coefficients. The overall procedure is described in the following subsections.

2.4.1 Problem variational statement

At a given load level, the discrete governing equations can be written starting from the statement of stationarity of the structure total potential energy

$$\delta\Pi = \delta U + \delta V = 0 \tag{26}$$

where U is the internal energy and V is the work done by the external forces.

Considering the plate kinematics and constitutive relations given in the above sections, the internal energy U may be written as

$$\begin{aligned} U &= \frac{1}{2}\int_\Omega \sum_{k=1}^{N_{ply}} \left\{ \int_{h_{k-1}}^{h_k} \left(\boldsymbol{e}_p^\intercal \boldsymbol{\sigma}_p + \boldsymbol{e}_n^\intercal \boldsymbol{\sigma}_n \right) dx_3 \right\} d\Omega = \\ &= \frac{1}{2}\int_\Omega \sum_{k=1}^{N_{ply}} \left\{ \int_{h_{k-1}}^{h_k} \left[\left(\boldsymbol{\varepsilon}^\intercal + x_3\boldsymbol{\kappa}^\intercal\right) \boldsymbol{Q}_p^{\langle k\rangle} \left(\boldsymbol{\varepsilon} + x_3\boldsymbol{\kappa}\right) + \boldsymbol{\gamma}^\intercal \boldsymbol{Q}_n^{\langle k\rangle} \boldsymbol{\gamma} \right] dx_3 \right\} d\Omega \end{aligned} \tag{27}$$

while the external work is given by

$$V = -\int_\Omega (\boldsymbol{u}^\intercal \boldsymbol{q} + \boldsymbol{\vartheta}^\intercal \boldsymbol{m}) d\Omega - \int_{\partial\Omega} \left(\boldsymbol{u}^\intercal \, \overline{\boldsymbol{N}} + \boldsymbol{\vartheta}^\intercal \, \overline{\boldsymbol{M}} \right) d\partial\Omega \tag{28}$$

where $\boldsymbol{q} = \{q_1, q_2, q_3\}^\intercal$ and $\boldsymbol{m} = \{m_1, m_2, 0\}^\intercal$ are the external forces and external moments per unit area applied over the domain Ω, whereas $\overline{\boldsymbol{N}}$ and $\overline{\boldsymbol{M}}$ denote prescribed forces and moments applied on the plate boundary $\partial\Omega_l \subset \partial\Omega$. The plate essential boundary conditions

are provided by prescribing the generalized displacements on the boundary $\partial\Omega_c$ as follows

$$\begin{aligned} \boldsymbol{\Xi}_u \boldsymbol{u} &= \boldsymbol{\Xi}_u \, \bar{\boldsymbol{u}} \quad \text{on } \partial\Omega_c \\ \boldsymbol{\Xi}_\vartheta \boldsymbol{\vartheta} &= \boldsymbol{\Xi}_\vartheta \, \bar{\boldsymbol{\vartheta}} \quad \text{on } \partial\Omega_c \end{aligned} \tag{29}$$

where $\boldsymbol{\Xi}_u$ and $\boldsymbol{\Xi}_\vartheta$ are boolean matrix operator used for selecting the desired constrained generalized displacements whereas the over-bar denotes prescribed quantities.

2.4.2 Ritz approximation

According to the Ritz solution scheme and following the work done in Refs. [16, 17], the discrete governing equations are obtained by approximating the generic component of generalized displacements $\chi \in \{u_1, u_2, u_3, \vartheta_1, \vartheta_2\}$ appearing in the variational statement in Eq.(26), through Eqs.(27-28), by a series of trial functions as

$$\chi = \sum_{m=1}^{M_\chi} \sum_{n=1}^{N_\chi} \psi_m(\xi) \, \psi_n(\eta) \, C_{\chi_{(m-1)M+n}} = \boldsymbol{\Psi}_\chi \boldsymbol{C}_\chi \tag{30}$$

where $\psi_m(\xi)$ and $\psi_n(\eta)$ denote 1D Legendre orthogonal polynomials of order m or n and $C_{\chi_{(m-1)M+n}}$ are the unknown Ritz coefficients. Eq.(30) can be specialized to the plate primary variables $\boldsymbol{u}$ and $\boldsymbol{\vartheta}$ and written in compact matrix form as

$$\boldsymbol{u} = \begin{bmatrix} \boldsymbol{\Psi}_{\boldsymbol{u_1}} & 0 & 0 \\ 0 & \boldsymbol{\Psi}_{\boldsymbol{u_2}} & 0 \\ 0 & 0 & \boldsymbol{\Psi}_{\boldsymbol{u_3}} \end{bmatrix} \begin{Bmatrix} \boldsymbol{C}_{u_1} \\ \boldsymbol{C}_{u_2} \\ \boldsymbol{C}_{u_3} \end{Bmatrix} = \begin{bmatrix} \boldsymbol{\Phi}_{u_1} \\ \boldsymbol{\Phi}_{u_2} \\ \boldsymbol{\Phi}_{u_3} \end{bmatrix} \boldsymbol{U} = \boldsymbol{\Phi}_u \boldsymbol{U} \tag{31}$$

and

$$\boldsymbol{\vartheta} = \begin{bmatrix} \boldsymbol{\Psi}_{\boldsymbol{\vartheta_1}} & 0 \\ 0 & \boldsymbol{\Psi}_{\boldsymbol{\vartheta_2}} \end{bmatrix} \begin{Bmatrix} \boldsymbol{C}_{\vartheta_1} \\ \boldsymbol{C}_{\vartheta_2} \end{Bmatrix} = \begin{bmatrix} \boldsymbol{\Phi}_{\vartheta_1} \\ \boldsymbol{\Phi}_{\vartheta_2} \end{bmatrix} \boldsymbol{\Theta} = \boldsymbol{\Phi}_\vartheta \boldsymbol{\Theta}. \tag{32}$$

Using the above equations, the in-plane strains vector $\boldsymbol{\varepsilon}$, the curvatures vector $\boldsymbol{\kappa}$ and the shear strains vector $\boldsymbol{\gamma}$ can be written as

$$\begin{aligned} \boldsymbol{\varepsilon} &= \boldsymbol{\mathcal{B}}_{pU} \boldsymbol{U} + \frac{1}{2} \boldsymbol{\mathcal{B}}_{nlU} \boldsymbol{U} + \bar{\boldsymbol{\mathcal{B}}}_{nlU} \boldsymbol{U}, \\ \boldsymbol{\kappa} &= \boldsymbol{\mathcal{B}}_{p\Theta} \boldsymbol{\Theta}, \qquad \boldsymbol{\gamma} = \boldsymbol{\mathcal{B}}_{nU} \boldsymbol{U} + \boldsymbol{\mathcal{B}}_{i\Theta} \boldsymbol{\Theta} \end{aligned} \tag{33}$$

where the operators $\boldsymbol{\mathcal{B}}$ are given in Appendix A.

2.4.3 Discrete equations and incremental solution

By considering Eqs.(31-32) and employing a penalty approach to enforce the essential boundary conditions, the stationarity condition $\delta\Pi = 0$ with respect to $\boldsymbol{U}$ and $\boldsymbol{\Theta}$ leads to the discrete system

$$
\begin{aligned}
&\int_\Omega \left[\left(\boldsymbol{\mathcal{B}}_{pU} + \boldsymbol{\mathcal{B}}_{nlU} + \bar{\boldsymbol{\mathcal{B}}}_{nlU}\right)^\intercal \boldsymbol{A} \left(\boldsymbol{\mathcal{B}}_{pU} + \frac{1}{2}\boldsymbol{\mathcal{B}}_{nlU} + \bar{\boldsymbol{\mathcal{B}}}_{nlU} \right) + \boldsymbol{\mathcal{B}}_{nU}^\intercal \boldsymbol{A}_s \boldsymbol{\mathcal{B}}_{nU} \right] \boldsymbol{U} d\Omega + \\
&+ \int_\Omega \left[\left(\boldsymbol{\mathcal{B}}_{pU} + \boldsymbol{\mathcal{B}}_{nlU} + \bar{\boldsymbol{\mathcal{B}}}_{nlU}\right)^\intercal \boldsymbol{B} \boldsymbol{\mathcal{B}}_{p\Theta} + \boldsymbol{\mathcal{B}}_{nU}^\intercal \boldsymbol{A}_s \boldsymbol{\mathcal{B}}_{i\Theta} \right] \boldsymbol{\Theta} d\Omega + \\
&+ \int_\Omega \left[\boldsymbol{\mathcal{B}}_{p\Theta}^\intercal \boldsymbol{B} \left(\boldsymbol{\mathcal{B}}_{pU} + \frac{1}{2}\boldsymbol{\mathcal{B}}_{nlU} + \bar{\boldsymbol{\mathcal{B}}}_{nlU} \right) + \boldsymbol{\mathcal{B}}_{i\Theta}^\intercal \boldsymbol{A}_s \boldsymbol{\mathcal{B}}_{nU} \right] \boldsymbol{U} d\Omega + \\
&+ \int_\Omega \left(\boldsymbol{\mathcal{B}}_{p\Theta}^\intercal \boldsymbol{D} \boldsymbol{\mathcal{B}}_{p\Theta} + \boldsymbol{\mathcal{B}}_{i\Theta}^\intercal \boldsymbol{A}_s \boldsymbol{\mathcal{B}}_{i\Theta} \right) \boldsymbol{\Theta} d\Omega + \\
&+ \int_{\partial\Omega_c} \left(\boldsymbol{\Phi}_u^\intercal \boldsymbol{\Xi}_u^\intercal \boldsymbol{\omega}_u \boldsymbol{\Xi}_u \boldsymbol{\Phi}_u \boldsymbol{U} + \boldsymbol{\Phi}_\vartheta^\intercal \boldsymbol{\Xi}_\vartheta^\intercal \boldsymbol{\omega}_\vartheta \boldsymbol{\Xi}_\vartheta \boldsymbol{\Phi}_\vartheta \boldsymbol{\Theta} \right) d\partial\Omega + \\
&= \int_\Omega \left(\boldsymbol{\Phi}_u^\intercal \boldsymbol{q} + \boldsymbol{\Phi}_\vartheta^\intercal \boldsymbol{m} \right) d\Omega + \int_{\partial\Omega_l} \left(\boldsymbol{\Phi}_u^\intercal \, \overline{\boldsymbol{N}} + \boldsymbol{\Phi}_\vartheta^\intercal \, \overline{\boldsymbol{M}} \right) d\partial\Omega + \\
&+ \int_{\partial\Omega_c} \left(\boldsymbol{\Phi}_u^\intercal \boldsymbol{\Xi}_u^\intercal \boldsymbol{\omega}_u \boldsymbol{\Xi}_u \boldsymbol{\Phi}_u \, \overline{\boldsymbol{u}} + \boldsymbol{\Phi}_\vartheta^\intercal \boldsymbol{\Xi}_\vartheta^\intercal \boldsymbol{\omega}_\vartheta \boldsymbol{\Xi}_\vartheta \boldsymbol{\Phi}_\vartheta \, \overline{\boldsymbol{\vartheta}} \right) d\partial\Omega,
\end{aligned}
\tag{34}
$$

which may be written in compact form as

$$
\left(\boldsymbol{K}_0 + \overline{\boldsymbol{K}}_0 + \boldsymbol{K}_1 + \boldsymbol{K}_2 + \overline{\boldsymbol{K}}_1 + \boldsymbol{R} \right) \boldsymbol{X} = \boldsymbol{F}_D + \boldsymbol{F}_L \tag{35}
$$

where $\boldsymbol{X} = \{\boldsymbol{U}, \boldsymbol{\Theta}\}^\intercal$ is the vector collecting the unknown coefficients of the Ritz series expansion, $\boldsymbol{K}_0$, $\boldsymbol{K}_1$, $\boldsymbol{K}_2$, $\overline{\boldsymbol{K}}_0$, $\overline{\boldsymbol{K}}_1$ are the stiffness matrices in which the subscripts 1,2 refer to the geometric non-linear terms and the over-bar refers to the prescribed initial imperfections, while $\boldsymbol{R}$ is the matrix originating from the enforcement of the BCs thorough a penalty approach. On the right hand-side, the vectors $\boldsymbol{F}_D$ and $\boldsymbol{F}_L$ collect the discrete terms associated with the external loads. Details on the matrices appearing in Eq.(35) are given in Appendix B.

To solve the non-linear problem given in Eq.(35), an incremental-iterative procedure is employed. It is important to observe that the local stiffness of the laminate layers, and thus all the matrices on the left hand-side of Eq.(35), except $\boldsymbol{R}$, are affected by the damage

level $\boldsymbol{\omega}[\mathscr{H}(\boldsymbol{X})]$. The vector $\boldsymbol{\omega}[\mathscr{H}(\boldsymbol{X})]$, which collects the damage indices, plays the role of an internal state vector that depends on the loading/solution history $\mathscr{H}(\boldsymbol{X})$. As a consequence, the incremental form of Eq.(35) may be expressed as

$$\boldsymbol{R}\,\Delta\boldsymbol{X} + \Delta\left[\left(\boldsymbol{K}_0 + \overline{\boldsymbol{K}}_0 + \boldsymbol{K}_1 + \boldsymbol{K}_2 + \overline{\boldsymbol{K}}_1\right)\boldsymbol{X}\right] = \Delta\boldsymbol{F}_D + \Delta\boldsymbol{F}_L \tag{36}$$

with

$$\Delta\left[\left(\boldsymbol{K}_0 + \overline{\boldsymbol{K}}_0 + \boldsymbol{K}_1 + \boldsymbol{K}_2 + \overline{\boldsymbol{K}}_1\right)\boldsymbol{X}\right] = \left(\boldsymbol{K}_{t,geo} + \boldsymbol{K}_{t,dmg}\right)\Delta\boldsymbol{X}, \tag{37}$$

where $\Delta\,(\circ)$ is the incremental operator, $\boldsymbol{K}_{t,geo}$ is the tangent stiffness matrix contribution related to the geometric non-linearity and the initial imperfections, whilst $\boldsymbol{K}_{t,dmg}$ is the tangent stiffness matrix contribution related to the damage evolution. Further details about such matrices are reported in Appendix C.

In this study, the non-linear damage evolution problem is solved employing an incremental-iterative Newton-Raphson scheme in displacement control. Once the solution at a given load step is obtained, a load increment is enforced, and the Newton-Raphson iteration is started, triggering the non-linear evolution of the internal damage variables; the process is arrested when the residual is reduced below a preset tolerance, so that a subsequent increment, if of interest, may be applied.

A relevant practical aspect is worth mentioning before describing the results of the proposed framework. Convergence issues are common and well-known in material models that exhibit softening and stiffness degradation. To alleviate such computational difficulties, in this work a viscous regularization scheme is adopted as suggested in Ref. [45]. The following evolution equation is then introduced

$$\dot{\omega}_i^v = \frac{1}{\beta}\left(\omega_i - \omega_i^v\right) \tag{38}$$

where β is a *viscous parameter* and ω_i^v denotes the regularized damaged variable for the *i-th* damage mode, computed as follow

$$\omega_i^v|_n = \frac{\Delta\tau}{\beta + \Delta\tau}\omega_i|_n + \frac{\beta}{\beta + \tau}\omega_i^v|_{n-1}, \tag{39}$$

where τ is the time/load parameter, the subscripts $n-1$ and n refer to two successive time/load steps, with $\Delta\tau$ denoting the increment between them. It is demonstrated that

using the viscous regularization scheme improves the rate of convergence without significantly compromising the results accuracy if the viscosity parameter β is small with respect to $\Delta\tau$.

3 Computational results

In this section, the developed computational framework is first validated through a convergence analysis and a comparison with available literature data. Then some analyses are performed for both classical and VAT laminates, considering both small and moderately large strains. The model proposed in Section 2 has been implemented using `MATLAB`® [46]. For all the performed analyses, the strain-softening parameter $\alpha_i = 2$ and the viscous parameter $\beta = 0.001$ have been selected for each damage index.

3.1 Method validation

The proposed model has been validated first by assessing its convergence with respect to the order of the polynomial expansions in the Ritz approximation given in Eq.(30). Then, two test cases have been analyzed, the first involving a plate that undergoes three-point bending loading in small strains and the second considering a plate subjected to a uni-axial in-plane compression and experiencing non-linear strains in the von Kármán sense.

The first analyzed case considers the rectangular composite straight-fibers plate schematically represented in Fig.(4), with sides of length $2a = 60\,\text{mm}$ and $2b = 25\,\text{mm}$, thickness $h = 1.8\,\text{mm}$. The unidirectional laminate is made up of M10 carbon/epoxy layers, whose material properties are listed in Tab.1, with $[0]_{10}$ laminate lay-up. The boundary conditions for the three-point bending test are defined so that, on the short edges, the rotation ϑ_1 and the in-plane displacements are free whilst the other degrees of freedom are fully constrained, whereas the longest edges are completely free.

The analysis has been performed in displacement control by increasing, at each step, the applied displacement Δu_3 of all the points of the center segment of the plate and employing a Newton-Raphson scheme. In the approximation of the generalized displacements given in Eqs.(31-32), the order of the adopted polynomial expansions was the same for all the kinematic variables, i.e. $M_\chi = N_\chi = p$. The convergence of the solution with respect to the degree of the polynomial expansion has been assessed by studying the total reaction

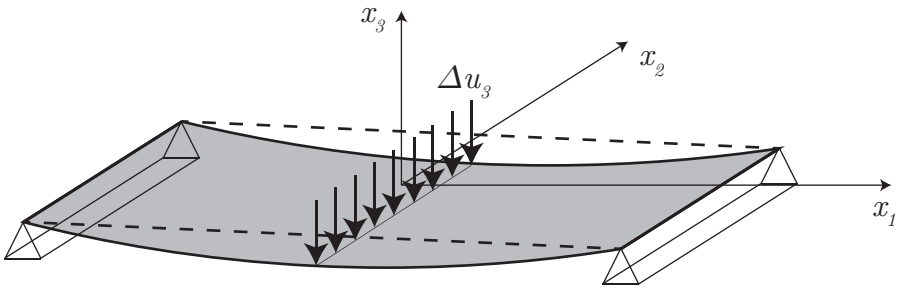

Figure 4: Schematic representation of three-point bending test.

Elastic property		Value	Strength property		Value
E_1	[GPa]	105.00	X_T	[MPa]	1400.0
E_2	[GPa]	8.57	X_C	[MPa]	930.0
$G_{23} = G_{13}$	[GPa]	3.05	Y_T	[MPa]	47.0
G_{12}	[GPa]	4.39	Y_C	[MPa]	60.3
ν_{12}		0.34	S_L	[MPa]	53.0

Table 1: Material properties of straight fiber lamina [47].

force along the x_3 direction at the supports and the displacement of the central point of the plate which is shown in Fig.(5a).

The analysis shows that, for the considered case, convergence is quickly achieved in the initial linear part of the response, whilst a relatively high number of polynomial expansion terms, up to the order $p = 30$, are needed to accurately represent the response in proximity of failure, as could be reasonably expected considering the localization of damage. The converged results, corresponding to $p = 30$, were then compared with experimental and FE results [34]. The analysis using the Ritz method with $p = 30$ has total of 4500 degrees of freedom (DOFs), whilst the FE results have been obtained using 2000 S8R elements with 49266 DOFs. As it can be observed in Fig.(5b), even if the proposed model underestimates the maximum load, it provides good agreement with the experimental test measurements.

The second analyzed case considers a quadrilateral quasi-isotropic composite plate with sides of length $2a = 2b = 250\,\text{mm}$ and thickness $h = 6\,\text{mm}$ subjected to uni-axial in-plane compression load along the x_1 direction, as schematically represented in Fig.(6).

The laminate is assembled from carbon/epoxy layers whose material properties are listed in Tab. 2, whilst its stacking sequence is $[0/90/45/-45]_S$. Also in this case a

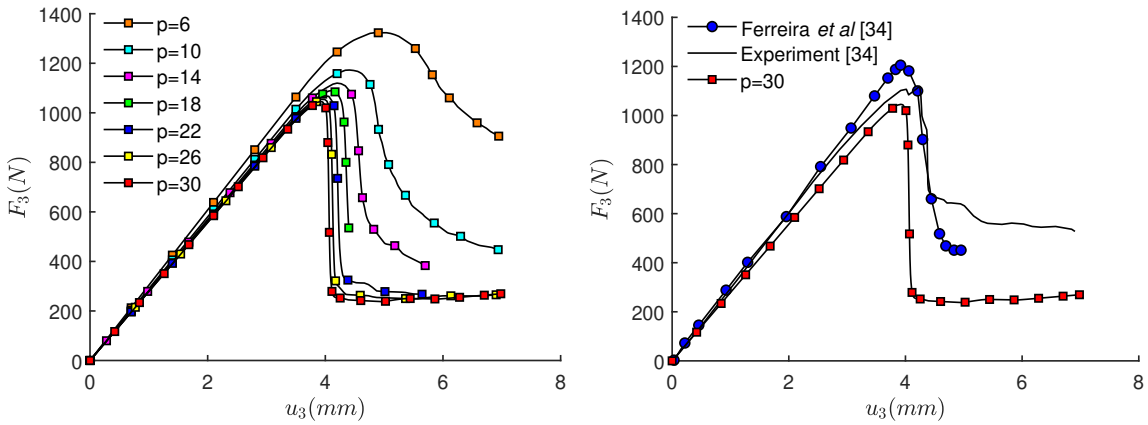

Figure 5: Three-point bending test of the unidirectional laminate response in terms of reaction force of supports vs transverse displacement at the center of the plate. (a) Convergence analysis and (b) comparison between the present model, experimental and FE results.

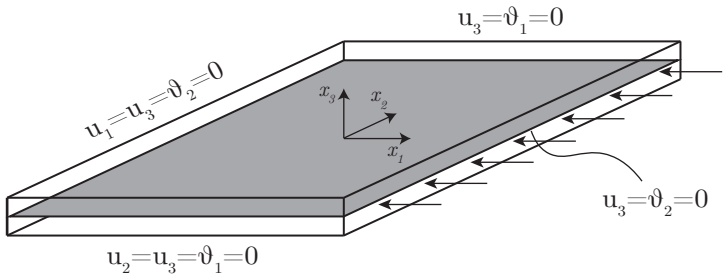

Figure 6: Schematic representation of the compressive test.

Elastic property		Value	Strength property		Value
E_1	[GPa]	181.00	X_T	[MPa]	1500.0
E_2	[GPa]	10.27	X_C	[MPa]	1200.0
G_{ij}	[GPa]	7.17	Y_T	[MPa]	40.0
ν_{12}		0.34	Y_C	[MPa]	176.0
			S_L	[MPa]	68.0

Table 2: Material properties of straight fiber lamina for compressive test, where $G_{ij} = G_{23} = G_{13} = G_{12}$.

convergence analysis has been first performed. To promote the plate lateral deflection before buckling, an initial imperfection is introduced as a bi-sinusoidal prescribed deflection with amplitude $0.005\,h$. The boundary conditions used in this analysis are reported in Table 3.

Fig.(7) shows the results of the convergence analysis in terms of transverse displacement of the plate's mid-plane center point versus the axial load value. The transverse displacement is normalized with respect to the plate thickness, whilst the axial load is normalized with respect to the critical buckling load [48]. In this case, results obtained with $p = 22$ do not significantly differ from those obtained with $p = 18$. Therefore, to perform faster analyses, the polynomial degree $p = 18$, which gives a total of 1620 DOFs, was used for the subsequent geometrically non-linear analyses involving comparable load cases. For validation purposes, Fig.(7) shows results from three different `ABAQUS` analyses, which are obtained using meshes of 20×20, 30×30 and 50×50 elements, respectively. For each mesh, S4R element type is considered, which gives a total of 2646, 5766 and 15606 DOFs, respectively. The FE results have been obtained employing an orthotropic damage model and adopting the built-in `ABAQUS` localization mitigation strategy, based on the crack-band theory. However, it is observed that, even adopting such scheme, the FE results show a relative scatter, which is consistent with several literature sources, see e.g. Ref. [49], which report that energy regularization strategies based on the crack band theory may partially lose objectivity for complex loading cases. It is also shown that, compared to the FE/`ABAQUS` results, the curves obtained by the proposed Ritz method exhibit reduced scatter and appear to converge with increasing polynomial order approximation.

Edge		u_1	u_2	u_3	ϑ_1	ϑ_2
$x_2 = -b,$	$x_1 \in [-a, a]$	F	C	C	C	F
$x_1 = +a,$	$x_2 \in (-b, b]$	F	F	C	F	C
$x_2 = +b,$	$x_1 \in (-a, a]$	F	F	C	C	F
$x_1 = -a,$	$x_2 \in [-b, b]$	C	F	C	F	C

Table 3: Boundary condition used for the convergence study of quasi-isotropic laminated. F=Free and C=Clamped.

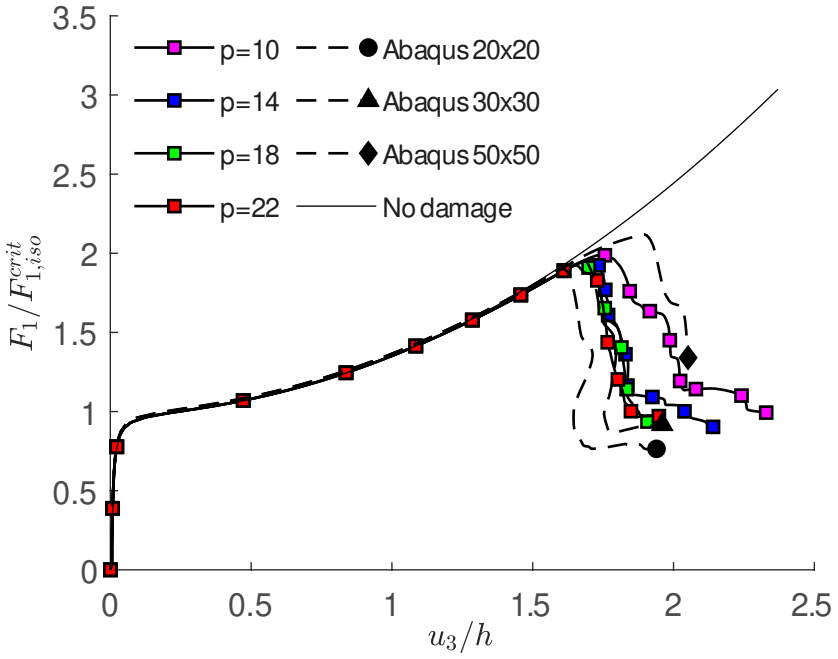

Figure 7: Convergence study of quasi-isotropic laminate under in-plane compressive load. Results obtained with the Ritz method are compared with FE/ABAQUS results for different discretizations.

3.2 Damage analysis of VAT laminates

After validation, the developed method has been applied to the analysis of VAT composite plates. VAT laminae are manufactured so that the reinforcing fibers follow curved paths, thus exhibiting varying angles with respect to structural reference directions. Such fiber paths can be described by specifying suitable laws for the fiber orientation θ. In this study, referring to Fig.(8), the following law is used

$$\theta = \theta_0 + \frac{\theta_A r_B - \theta_B r_A}{r_B - r_A} + |r| \frac{\theta_B - \theta_A}{r_B - r_A} \tag{40}$$

where θ_0 is the angle between the baseline and the axis x_1, θ_A and θ_B measure the angle of the fibers at the points A and B, whilst r_A and r_B are the distances of these points from the projection O' of the plate center on the baseline. Following the notation used in Ref. [9], the point A is assumed to be coincident with the plate center point projection O' and $r_B = 2a$, so that the law describing the fiber path of a lamina can be denoted as $\theta_0 + \langle \theta_A | \theta_B \rangle$. In the application of the developed Ritz scheme to VAT laminates, the stiffness contributions are computed considering the local variation of the materials properties induced by the local fibers orientation.

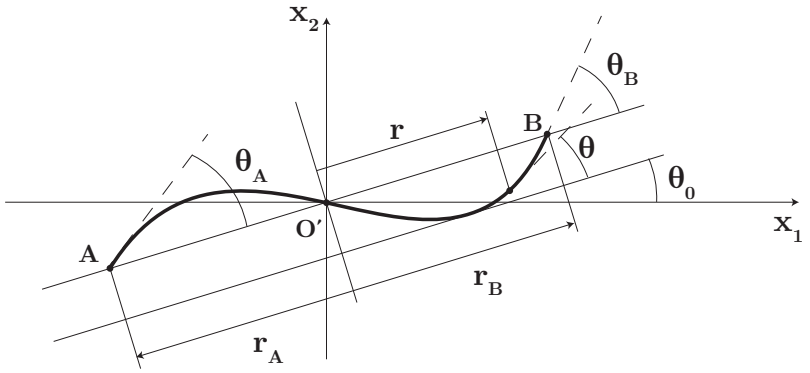

Figure 8: Geometric description of VAT lamina for fiber orientation definition.

The first test considers a VAT composite plate with stacking sequence $[0 + \langle 0| - 90\rangle/0 + \langle 90|0\rangle/0]_S$ under tensile loading. The material properties for each lamina with respect to the fiber and transverse directions are given again in Table 2. The plate has sides of size $2a = 2b = 250\,\text{mm}$ and thickness $h = 6.25\,\text{mm}$.

Fig.(9) shows the response in terms of force vs displacement along the x_1 direction. As expected, after the load reaches a maximum level, it suddenly drops while the damage level in each ply rises. Referring to Fig.(9), four points of interest along the loading curve are highlighted: point A identifies the initiation of damage; point B corresponds to the maximum load; points C and D describe the post-failure load drop.

The contour plots of the relevant damage indexes corresponding to the four highlighted points are reported in Fig.(10), which describes how damage evolves through the thickness during the loading process. It is worth noting that only the results for the first three plies are shown, considering the symmetry of the laminate. At point A, matrix tension damage initiates in the first two plies, whereas the 0° ply is still undamaged. When the maximum load is attained, at point B, damage has spread through the thickness in all the laminae. Next, in proximity of the sudden load drop, damage still evolves in all the plies, as can be seen for point C, before eventually reaching the maximum level at point D.

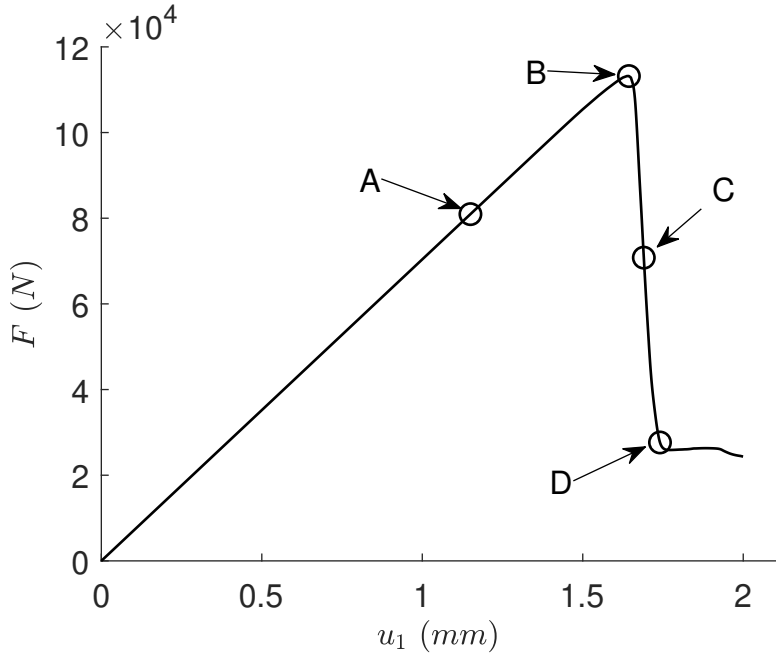

Figure 9: Force vs displacement results for VAT laminate under tensile load.

After considering a VAT laminated plate in tension, for which a small strains implementation has been employed, some VAT laminates under compression loading are analyzed,

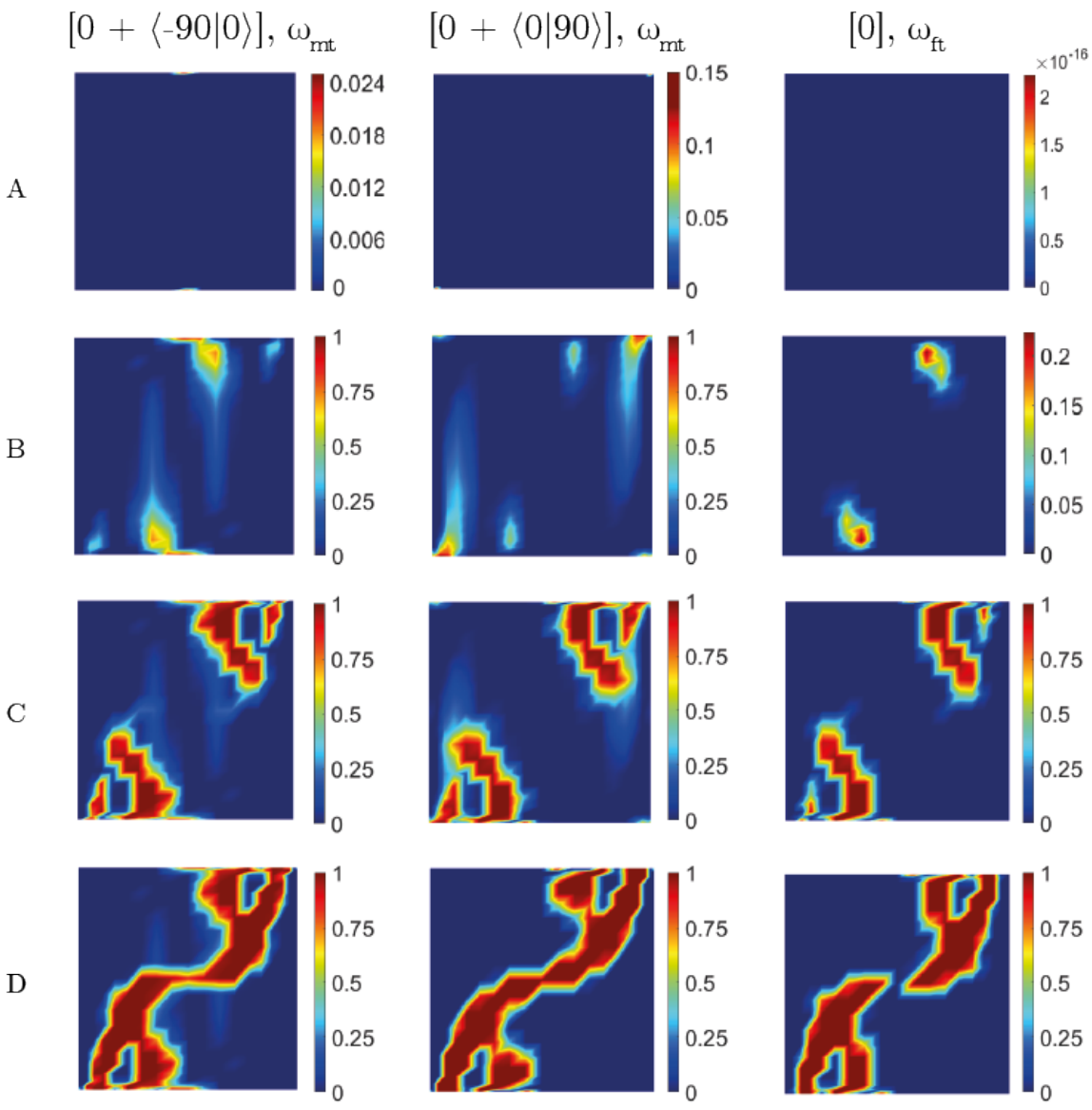

Figure 10: Damage contour plots for 3 plies of a VAT laminate laminate under tensile test at points of interest.

activating the presence of moderate strains in the von Kármán sense.

Square plates with sides of size $a = b = 250\,\text{mm}$ are considered. Four lay-ups, namely $[90\pm\langle 0|75\rangle]_{3S}$, $[0\pm\langle 0|15\rangle]_{3S}$, $[0\pm\langle 0|45\rangle]_{3S}$, $[0\pm\langle 45|0\rangle]_{3S}$ are investigated. They consist of 12 constant thickness plies, each 0.27 mm thick. The material properties for each orthotropic

layer, along the fibers and transverse directions, are summarised in Table 2. The panels are loaded by uniform axial displacement imposed along the edges parallel to the x_2 axis and an initial prescribed lateral bi-sinusoidal deflection of amplitude $0.005\,h$ has been introduced, where h indicates the plate thickness. Simply-supported boundary conditions are assumed for all the edges, with free in-plane displacements allowed along the unloaded edges, as reported in Fig.(11).

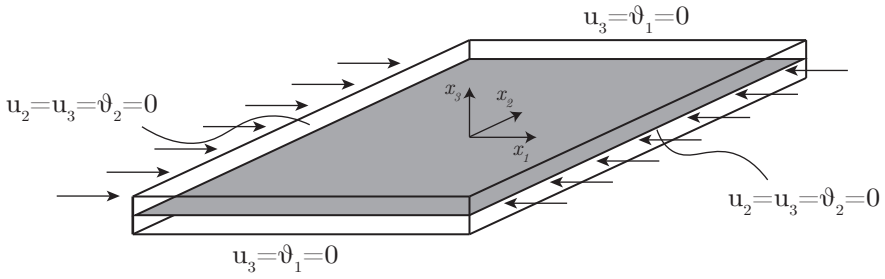

Figure 11: Schematic representation of the VAT composite under compressive load.

Fig.(12) shows the comparison in terms of in-plane force versus plate center deflection for different VAT plate stacking sequences. The force has been normalized with respect to the critical buckling load of a quasi-isotropic laminate of the same size while the transverse displacement has been normalized with respect to the laminate thickness.

The results show that, as expected, the presence of damage affects the mechanical response of the plate, identifying a maximum load after which the bearing capability of the plate is noticeably degraded. Such results may be useful for identifying the operational limits of different lay-ups, thus providing valuable insights to the designer.

4 Discussion

In this section, some remarks about the potential, limitations and future developments of the method are discussed.

The formulation provides meaningful insights about the damage initiation, evolution and failure of composite laminates, including VAT configurations, at a relatively moderate computational cost in terms of number of DOFs. The tool may be valuable for identifying the operational limits of structural components in damage-tolerant approaches, since the

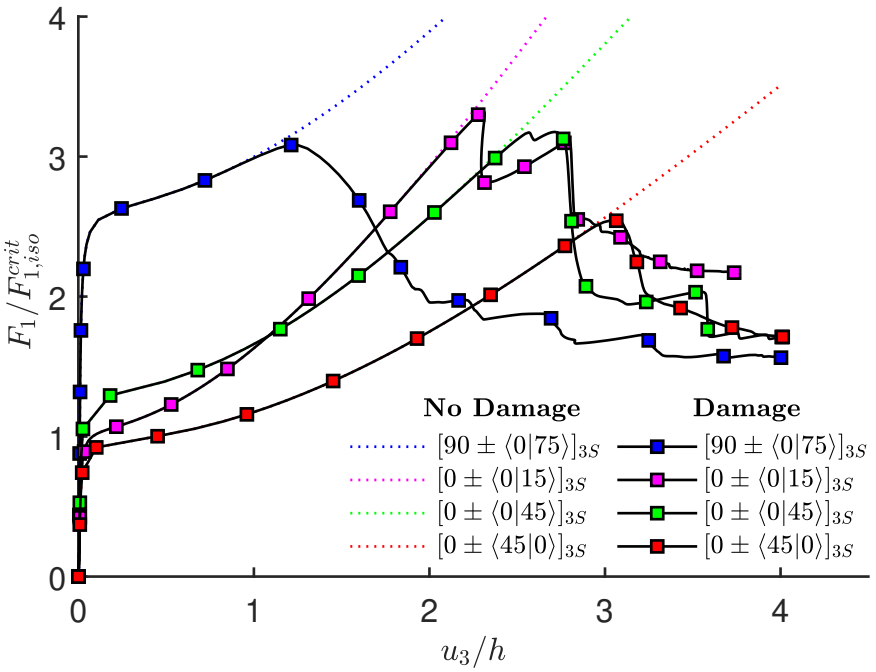

Figure 12: Comparison of post-buckling results in terms of force vs transverse displacement with and without the damage model activated for different VAT layups under in plane-load.

preliminary design stage. Moreover, it simplifies the data preparation stage of the analysis, as it frees the user from the need of preparing a suitable mesh for capturing the features of the VAT plates, which may require a noticeable amount of time and attention. In the present model, only the polynomial order must be selected according to the features of the underlying problem. The obtained results have shown an appreciable qualitative consistency with available literature data and with finite element computations. However, some aspects deserve further analysis and provide input for further studies.

First, the behavior of the method with respect to damage localization issues and contingent dependency of the macro structural response on the order of the Ritz polynomial expansion should be further investigated. This analysis would be the counterpart of the investigations on spurious mesh dependency in FE models, which gave rise to either local or non-local approaches for ensuring the objectivity of the computational response with respect to mesh refinements, such as the crack-band theory [50] or non-local integral models [51]. From this point of view, the performed analyses have shown the convergence of the results towards a well defined response; in a certain sense, the Ritz approximation shows the features of non-local approaches, being the integration extended over all the analysis domain, so that some damage *smearing* naturally occurs.

The above aspects have been considered in performing the proposed test cases. However, their deeper analysis is left for further investigations. Other relevant aspects, in this context, are related to the *resolution* afforded by the proposed approach and to the assessment of the possible presence of spurious effects as those related, for example, to Gibbs effects.

From a more physical point of view, the model could be extended considering other damage mechanisms such as inter-laminar delamination or impact induced damage. Delamination could be modelled by using layer-wise displacement approximations along the thickness, hybrid variational statements [52], and cohesive inter-laminar traction-separation laws [53, 54]. These tools would provide a direct representation of the displacement jumps between contiguous layers and their relation with the inter-laminar damage up to complete decohesion. Impact-induced damage could be investigated employing suitable contact mechanics laws for representing the localized mechanical effects of impacts in conjunction with the incremental scheme proposed here, to track the ensuing damage evolution [55].

Eventually, the model could be extended to account for generally large strains, overcoming the von Kármán assumption. This would provide the basis for analyzing cases

involving highly non-linear deformation patterns, relevant for the study of soft materials, which are attracting ever increasing attention.

5 Conclusions

A non-linear Ritz approach for the analysis damage initiation and evolution up to failure of VAT composite plates under progressive loading has been developed, implemented and tested. The present study has detailed the formulation of the method, which addresses both geometrical non-linearity, in the form of moderate von Kármán strains, and material non-linearity, in the form of material degradation, modeled as softening in the framework of continuum damage mechanics. A set of tests has successfully validated the implemented model against available literature data, provided either by FE or experimental results. Some original analyses have been reported for the post-buckling analysis of composite VAT laminated plates in presence of damage. The reported tests confirm the potential of the method; few directions of further investigation have been identified and discussed.

6 Acknowledgments

The Authors gratefully acknowledge the support of the PON Ricerca e Innovazione 2014-2020 – Fondo Sociale Europeo, Azione I.1 *Dottorati Innovativi con caratterizzazione Industriale* – Ciclo XXXVI (CUP: B73D20005010001 – Scholarship ID: DOT20KTEXX). I.B. also acknowledges the support of the Department of Engineering of the University of Palermo through the grant *Premio gruppo di ricerca 2020*.

References

[1] C. Kassapoglou, *Applications of Advanced Composites in Aircraft Structures*, ch. 1, pp. 1–7. John Wiley & Sons, Ltd, 2013.

[2] P. Parandoush and D. Lin, "A review on additive manufacturing of polymer-fiber composites," *Composite Structures*, vol. 182, pp. 36–53, 2017.

[3] K. Yassin and M. Hojjati, "Processing of thermoplastic matrix composites through automated fiber placement and tape laying methods: A review," *Journal of Thermoplastic Composite Materials*, vol. 31, no. 12, pp. 1676–1725, 2018.

[4] V. Oliveri, G. Zucco, D. Peeters, G. Clancy, R. Telford, M. Rouhi, C. McHale, R. M. O'Higgins, T. M. Young, and P. M. Weaver, "Design, manufacture and test of an in-situ consolidated thermoplastic variable-stiffness wingbox," *AIAA Journal*, vol. 57, no. 4, pp. 1671–1683, 2019.

[5] V. Dhinakaran, K. Surendar, M. Hasunfur Riyaz, and M. Ravichandran, "Review on study of thermosetting and thermoplastic materials in the automated fiber placement process," *Materials Today: Proceedings*, vol. 27, pp. 812–815, 2020. First International conference on Advanced Lightweight Materials and Structures.

[6] M. Hyer and H. Lee, "The use of curvilinear fiber format to improve buckling resistance of composite plates with central circular holes," *Composite Structures*, vol. 18, no. 3, pp. 239–261, 1991.

[7] G. G. Lozano, A. Tiwari, C. Turner, and S. Astwood, "A review on design for manufacture of variable stiffness composite laminates," *Proceedings of the Institution of Mechanical Engineers, Part B: Journal of Engineering Manufacture*, vol. 230, no. 6, pp. 981–992, 2016.

[8] Z. Gurdal and R. Olmedo, "In-plane response of laminates with spatially varying fiber orientations - Variable stiffness concept," *AIAA Journal*, vol. 31, no. 4, pp. 751–758, 1993.

[9] Z. Gürdal, B. Tatting, and C. Wu, "Variable stiffness composite panels: Effects of stiffness variation on the in-plane and buckling response," *Composites Part A: Applied Science and Manufacturing*, vol. 39, no. 5, pp. 911–922, 2008.

[10] Z. Wu, P. M. Weaver, G. Raju, and B. Chul Kim, "Buckling analysis and optimisation of variable angle tow composite plates," *Thin-Walled Structures*, vol. 60, pp. 163–172, 2012.

[11] E. Carrera, "Theories and finite elements for multilayered, anisotropic, composite plates and shells," *Archives of Computational Methods in Engineering*, vol. 9, no. 2, pp. 87–140, 2002.

[12] M. F. Caliri Jr, A. J. Ferreira, and V. Tita, "A review on plate and shell theories for laminated and sandwich structures highlighting the finite element method," *Composite Structures*, vol. 156, pp. 63–77, 2016.

[13] L. Demasi, G. Biagini, F. Vannucci, E. Santarpia, and R. Cavallaro, "Equivalent single layer, zig-zag, and layer wise theories for variable angle tow composites based on the generalized unified formulation," *Composite Structures*, vol. 177, pp. 54–79, 2017.

[14] V. Gulizzi, I. Benedetti, and A. Milazzo, "An implicit mesh discontinuous galerkin formulation for higher-order plate theories," *Mechanics of Advanced Materials and Structures*, vol. 27, no. 17, pp. 1494–1508, 2020.

[15] K. Liew, X. Zhao, and A. J. Ferreira, "A review of meshless methods for laminated and functionally graded plates and shells," *Composite Structures*, vol. 93, no. 8, pp. 2031–2041, 2011.

[16] A. Milazzo and V. Oliveri, "Buckling and postbuckling of stiffened composite panels with cracks and delaminations by ritz approach," *AIAA Journal*, vol. 55, no. 3, pp. 965–980, 2017.

[17] V. Oliveri and A. Milazzo, "A rayleigh-ritz approach for postbuckling analysis of variable angle tow composite stiffened panels," *Computers & Structures*, vol. 196, pp. 263–276, 2018.

[18] A. Milazzo, I. Benedetti, and V. Gulizzi, "An extended ritz formulation for buckling and post-buckling analysis of cracked multilayered plates," *Composite Structures*, vol. 201, pp. 980–994, 2018.

[19] A. Milazzo, I. Benedetti, and V. Gulizzi, "A single-domain ritz approach for buckling and post-buckling analysis of cracked plates," *International Journal of Solids and Structures*, vol. 159, pp. 221–231, 2019.

[20] G. Sciascia, V. Oliveri, and P. M. Weaver, "Eigenfrequencies of prestressed variable stiffness composite shells," *Composite Structures*, vol. 270, p. 114019, 2021.

[21] G. Sciascia, V. Oliveri, and P. M. Weaver, "Dynamic analysis of prestressed variable stiffness composite shell structures," *Thin-Walled Structures*, vol. 175, p. 109193, 2022.

[22] C. González and J. LLorca, "Mechanical behavior of unidirectional fiber-reinforced polymers under transverse compression: Microscopic mechanisms and modeling," *Composites Science and Technology*, vol. 67, no. 13, pp. 2795–2806, 2007.

[23] M. Lo Cascio, A. Milazzo, and I. Benedetti, "Virtual element method for computational homogenization of composite and heterogeneous materials," *Composite Structures*, vol. 232, p. 111523, 2020.

[24] M. Lo Cascio, A. Milazzo, and I. Benedetti, "A hybrid virtualâ–boundary element formulation for heterogeneous materials," *International Journal of Mechanical Sciences*, vol. 199, p. 106404, 2021.

[25] M. Lo Cascio and I. Benedetti, "Coupling bem and vem for the analysis of composite materials with damage," *Journal of Multiscale Modelling*, vol. 13, no. 01, p. 2144001, 2022.

[26] V. Gulizzi, V. Oliveri, and A. Milazzo, "Buckling and post-buckling analysis of cracked stiffened panels via an x-ritz method," *Aerospace Science and Technology*, vol. 86, pp. 268–282, 2019.

[27] V. Gulizzi, I. Benedetti, and A. Milazzo, "A novel boundary element formulation for anisotropic fracture mechanics," *Theoretical and Applied Fracture Mechanics*, vol. 104, p. 102329, 2019.

[28] A. Matzenmiller, J. Lubliner, and R. Taylor, "A constitutive model for anisotropic damage in fiber-composites," *Mechanics of Materials*, vol. 20, pp. 125–152, 1995.

[29] P. Ladeveze and E. LeDantec, "Damage modelling of the elementary ply for laminated composites," *Composites Science and Technology*, vol. 43, no. 3, pp. 257–267, 1992.

[30] I. Benedetti, H. Nguyen, R. A. Soler-Crespo, W. Gao, L. Mao, A. Ghasemi, J. Wen, S. Nguyen, and H. D. Espinosa, "Formulation and validation of a reduced order model of 2d materials exhibiting a two-phase microstructure as applied to graphene oxide," *Journal of the Mechanics and Physics of Solids*, vol. 112, pp. 66–88, 2018.

[31] I. Benedetti and M. Aliabadi, "Multiscale modeling of polycrystalline materials: A boundary element approach to material degradation and fracture," *Computer Methods in Applied Mechanics and Engineering*, vol. 289, pp. 429–453, 2015.

[32] P. Maimí, P. Camanho, J. Mayugo, and C. Dávila, "A continuum damage model for composite laminates: Part i - constitutive model," *Mechanics of Materials*, vol. 39, pp. 897 – 908, 2007.

[33] P. Maimí, P. Camanho, J. Mayugo, and C. Dávila, "A continuum damage model for composite laminates: Part ii - computational implementation and validation," *Mechanics of Materials*, vol. 39, pp. 909 – 919, 2007.

[34] G. F. Ferreira, J. H. S. Almeida, M. L. Ribeiro, A. J. Ferreira, and V. Tita, "A finite element unified formulation for composite laminates in bending considering progressive damage," *Thin-Walled Structures*, vol. 172, p. 108864, 2022.

[35] C. Lopes, P. Camanho, Z. Gürdal, and B. Tatting, "Progressive failure analysis of tow-placed, variable-stiffness composite panels," *International Journal of Solids and Structures*, vol. 44, no. 25, pp. 8493–8516, 2007.

[36] P. Ladevèze, O. Allix, L. Gornet, D. Lévêque, and L. Perret, "A computational damage mechanics approach for laminates: identification and comparison with experimental results," in *Studies in Applied Mechanics*, vol. 46, pp. 481–500, Elsevier, 1998.

[37] B. Falzon and P. Apruzzese, "Numerical analysis of intralaminar failure mechanisms in composite structures. part i: Fe implementation," *Composite Structures*, vol. 93, no. 2, pp. 1039–1046, 2011.

[38] B. Falzon and P. Apruzzese, "Numerical analysis of intralaminar failure mechanisms in composite structures. part ii: Applications," *Composite Structures*, vol. 93, no. 2, pp. 1047–1053, 2011.

[39] Q. J. Yang and B. Hayman, "Simplified ultimate strength analysis of compressed composite plates with linear material degradation," *Composites Part B: Engineering*, vol. 69, pp. 13–21, 2015.

[40] Q. J. Yang and B. Hayman, "Prediction of post-buckling and ultimate compressive strength of composite plates by semi-analytical methods," *Engineering Structures*, vol. 84, pp. 42–53, 2015.

[41] J.N.Reddy, *Mechanics of Laminated Composite Plates and Shells: Theory and Analysis*. CRC Press, 2nd ed., 2003.

[42] Z. Hashin and A. Rotem, "A fatigue failure criterion for fiber reinforced materials," *Journal of Composite Materials*, vol. 7, no. 4, pp. 448–464, 1973.

[43] Z. Hashin, "Failure criteria for unidirectional fiber composites," *Journal of Applied Mechanics*, vol. 47, no. 2, pp. 329–334, 1980.

[44] X. Deng, A. Korobenko, J. Yan, and Y. Bazilevs, "Isogeometric analysis of continuum damage in rotation-free composite shells," *Computer Methods in Applied Mechanics and Engineering*, vol. 284, pp. 349–372, 2015.

[45] I. Lapczyk and J. A. Hurtado, "Progressive damage modeling in fiber-reinforced materials," *Composites: Part A*, vol. 38, p. 2333–2341, 2007.

[46] MATLAB, *9.10.0.1710957 (R2021a) Update 4*. Natick, Massachusetts: The MathWorks Inc., 2021.

[47] V. Tita, J. de Carvalho, and D. Vandepitte, "Failure analysis of low velocity impact on thin composite laminates: Experimental and numerical approaches," *Composite Structures*, vol. 83, no. 4, pp. 413–428, 2008.

[48] C. G. Diaconu and P. M. Weaver, "Approximate solution and optimum design of compression-loaded, postbuckled laminated composite plates," *AIAA Journal*, vol. 43, no. 4, pp. 906–914, 2005.

[49] B. Lopes, M. Arruda, L. Almeida-Fernandes, L. Castro, N. Silvestre, and J. Correia, "Assessment of mesh dependency in the numerical simulation of compact tension tests for orthotropic materials," *Composites Part C: Open Access*, vol. 1, p. 100006, 2020.

[50] Z. P. Bažant and B. H. Oh, "Crack band theory for fracture of concrete," *Matériaux et construction*, vol. 16, no. 3, pp. 155–177, 1983.

[51] Z. P. Bažant and M. Jirásek, "Nonlocal integral formulations of plasticity and damage: Survey of progress," *Journal of Engineering Mechanics*, vol. 128, no. 11, pp. 1119–1149, 2002.

[52] I. Benedetti and A. Milazzo, "Advanced models for smart multilayered plates based on reissner mixed variational theorem," *Composites Part B: Engineering*, vol. 119, pp. 215–229, 2017.

[53] I. Benedetti and M. Aliabadi, "A three-dimensional cohesive-frictional grain-boundary micromechanical model for intergranular degradation and failure in polycrystalline materials," *Computer Methods in Applied Mechanics and Engineering*, vol. 265, pp. 36–62, 2013.

[54] F. Parrinello and I. Benedetti, "A coupled plasticity-damage cohesive-frictional interface for low-cycle fatigue analysis," *International Journal of Mechanical Sciences*, vol. 224, p. 107298, 2022.

[55] A. Milazzo and I. Benedetti, "A non-linear ritz method for the analysis of low velocity impact induced dynamics in variable angle tow composite laminates," *Composite Structures*, vol. 276, 2021.

A Ritz discrete operators

The discrete Ritz operators appearing in Eq.(33) are given by

$$\begin{aligned}
&\boldsymbol{\mathcal{B}}_{pU} = \boldsymbol{\mathcal{D}}_p \boldsymbol{\Phi}_u && \\
&\boldsymbol{\mathcal{B}}_{nU} = \boldsymbol{\mathcal{D}}_n \boldsymbol{\Phi}_u && \bar{\boldsymbol{\mathcal{B}}}_{nlU} = [\boldsymbol{\mathcal{D}}_p \otimes \overline{w}]\, \boldsymbol{\mathcal{D}}_n \boldsymbol{\Phi}_u \\
&\boldsymbol{\mathcal{B}}_{p\Theta} = \boldsymbol{\mathcal{D}}_p \boldsymbol{\Phi}_\vartheta && \boldsymbol{\mathcal{B}}_{nlU} = [\boldsymbol{\mathcal{D}}_p \otimes (\boldsymbol{\Phi}_{u_3} \boldsymbol{U})]\, \boldsymbol{\mathcal{D}}_n \boldsymbol{\Phi}_u \\
&\boldsymbol{\mathcal{B}}_{i\Theta} = \boldsymbol{\Phi}_\vartheta &&
\end{aligned} \tag{41}$$

B Governing equation matrices

The matrices appearing in Eq.(35) have the following expressions

$$\boldsymbol{K}_0 = \int_\Omega \begin{bmatrix} \left(\boldsymbol{\mathcal{B}}_{pU}^\intercal \boldsymbol{A} \boldsymbol{\mathcal{B}}_{pU} + \boldsymbol{\mathcal{B}}_{nU}^\intercal \boldsymbol{A}_s \boldsymbol{\mathcal{B}}_{nU}\right) & \left(\boldsymbol{\mathcal{B}}_{pU}^\intercal \boldsymbol{B} \boldsymbol{\mathcal{B}}_{p\Theta} + \boldsymbol{\mathcal{B}}_{nU} \boldsymbol{A}_s \boldsymbol{\mathcal{B}}_{i\Theta}\right) \\ \left(\boldsymbol{\mathcal{B}}_{p\Theta}^\intercal \boldsymbol{B} \boldsymbol{\mathcal{B}}_{pU} + \boldsymbol{\mathcal{B}}_{i\Theta}^\intercal \boldsymbol{A}_s \boldsymbol{\mathcal{B}}_{nU}\right) & \left(\boldsymbol{\mathcal{B}}_{p\Theta}^\intercal \boldsymbol{D} \boldsymbol{\mathcal{B}}_{p\Theta} + \boldsymbol{\mathcal{B}}_{i\Theta} \boldsymbol{A}_s \boldsymbol{\mathcal{B}}_{i\Theta}\right) \end{bmatrix} d\Omega,$$

$$\boldsymbol{K}_1 = \frac{1}{2} \int_\Omega \begin{bmatrix} \left(\boldsymbol{\mathcal{B}}_{pU}^\intercal \boldsymbol{A} \boldsymbol{\mathcal{B}}_{nlU} + \boldsymbol{\mathcal{B}}_{nlU}^\intercal \boldsymbol{A} \boldsymbol{\mathcal{B}}_{pU}\right) & 2\boldsymbol{\mathcal{B}}_{nlU}^\intercal \boldsymbol{B} \boldsymbol{\mathcal{B}}_{p\Theta} \\ \boldsymbol{\mathcal{B}}_{p\Theta}^\intercal \boldsymbol{B} \boldsymbol{\mathcal{B}}_{nlU} & 0 \end{bmatrix} d\Omega,$$

$$\boldsymbol{K}_2 = \frac{1}{2} \int_\Omega \begin{bmatrix} \boldsymbol{\mathcal{B}}_{nlU}^\intercal \boldsymbol{A} \boldsymbol{\mathcal{B}}_{nlU} & 0 \\ 0 & 0 \end{bmatrix} d\Omega,$$

$$\overline{\boldsymbol{K}}_0 = \int_\Omega \begin{bmatrix} \left(\boldsymbol{\mathcal{B}}_{pU}^\intercal \boldsymbol{A} \bar{\boldsymbol{\mathcal{B}}}_{nlU} + \bar{\boldsymbol{\mathcal{B}}}_{nlU}^\intercal \boldsymbol{A} \boldsymbol{\mathcal{B}}_{pU} + \bar{\boldsymbol{\mathcal{B}}}_{nlU}^\intercal \boldsymbol{A} \bar{\boldsymbol{\mathcal{B}}}_{nlU}\right) & \bar{\boldsymbol{\mathcal{B}}}_{nlU}^\intercal \boldsymbol{B} \boldsymbol{\mathcal{B}}_{p\Theta} \\ \boldsymbol{\mathcal{B}}_{p\Theta}^\intercal \boldsymbol{B} \bar{\boldsymbol{\mathcal{B}}}_{nlU} & 0 \end{bmatrix} d\Omega,$$

$$\overline{\boldsymbol{K}}_1 = \frac{1}{2} \int_\Omega \begin{bmatrix} \left(2\boldsymbol{\mathcal{B}}_{nlU}^\intercal \boldsymbol{A} \bar{\boldsymbol{\mathcal{B}}}_{nlU} + \bar{\boldsymbol{\mathcal{B}}}_{nlU}^\intercal \boldsymbol{A} \boldsymbol{\mathcal{B}}_{nlU}\right) & 0 \\ 0 & 0 \end{bmatrix} d\Omega, \tag{42}$$

$$\boldsymbol{R} = \int_\Omega \begin{bmatrix} \boldsymbol{\Phi}_u^\intercal \boldsymbol{\Xi}_u^\intercal \boldsymbol{\omega}_u \boldsymbol{\Xi}_u \boldsymbol{\Phi}_u & 0 \\ 0 & \boldsymbol{\Phi}_\vartheta^\intercal \boldsymbol{\Xi}_\vartheta^\intercal \boldsymbol{\omega}_\vartheta \boldsymbol{\Xi}_\vartheta \boldsymbol{\Phi}_\vartheta \end{bmatrix} d\Omega,$$

$$\boldsymbol{F}_L = \int_\Omega \begin{Bmatrix} \boldsymbol{\Phi}_u^\intercal \boldsymbol{q} \\ \boldsymbol{\Phi}_\vartheta^\intercal \boldsymbol{m} \end{Bmatrix} d\Omega + \int_{\partial\Omega_l} \begin{Bmatrix} \boldsymbol{\Phi}_u^\intercal \, \overline{\boldsymbol{N}} \\ \boldsymbol{\Phi}_\vartheta^\intercal \, \overline{\boldsymbol{M}} \end{Bmatrix} d\partial\Omega,$$

$$\boldsymbol{F}_D = \int_{\partial\Omega_c} \begin{Bmatrix} \boldsymbol{\Phi}_u^\intercal \boldsymbol{\Xi}_u^\intercal \boldsymbol{\omega}_u \boldsymbol{\Xi}_u \, \bar{\boldsymbol{u}} \\ \boldsymbol{\Phi}_\vartheta^\intercal \boldsymbol{\Xi}_\vartheta^\intercal \boldsymbol{\omega}_\vartheta \boldsymbol{\Xi}_\vartheta \, \bar{\boldsymbol{\vartheta}} \end{Bmatrix} d\partial\Omega.$$

C Tangent stiffness matrix contributions

The tangent stiffness matrix contribution $\boldsymbol{K}_{t,geo}$, related to the geometric non-linearity in Eq.(37), is computed as

$$\boldsymbol{K}_{t,geo} = \boldsymbol{K}_{1t} + \overline{\boldsymbol{K}}_{1t} + \boldsymbol{K}_{2t} + \boldsymbol{K}_G, \tag{43}$$

where the matrices $\boldsymbol{K}_{1t}$, $\boldsymbol{K}_{2t}$, $\overline{\boldsymbol{K}}_{1t}$ and $\boldsymbol{K}_G$ are defined as

$$\boldsymbol{K}_{1t} = \int_\Omega \begin{bmatrix} \left(\boldsymbol{\mathcal{B}}_{pU}^\intercal \boldsymbol{A} \boldsymbol{\mathcal{B}}_{nlU} + \boldsymbol{\mathcal{B}}_{nlU}^\intercal \boldsymbol{A} \boldsymbol{\mathcal{B}}_{pU}\right) & \boldsymbol{\mathcal{B}}_{nlU}^\intercal \boldsymbol{B} \boldsymbol{\mathcal{B}}_{p\Theta} \\ \boldsymbol{\mathcal{B}}_{p\Theta}^\intercal \boldsymbol{B} \boldsymbol{\mathcal{B}}_{nlU} & 0 \end{bmatrix} d\Omega,$$

$$\overline{\boldsymbol{K}}_{1t} = \int_\Omega \begin{bmatrix} \left(\boldsymbol{\mathcal{B}}_{nlU}^\intercal \boldsymbol{A} \bar{\boldsymbol{\mathcal{B}}}_{nlU} + \bar{\boldsymbol{\mathcal{B}}}_{nlU}^\intercal \boldsymbol{A} \boldsymbol{\mathcal{B}}_{nlU}\right) & 0 \\ 0 & 0 \end{bmatrix} d\Omega, \tag{44}$$

$$\boldsymbol{K}_{2t} = \int_\Omega \begin{bmatrix} \boldsymbol{\mathcal{B}}_{nlU}^\intercal \boldsymbol{A} \boldsymbol{\mathcal{B}}_{nlU} & 0 \\ 0 & 0 \end{bmatrix} d\Omega, \qquad \boldsymbol{K}_G = \int_\Omega \begin{bmatrix} \boldsymbol{\mathcal{B}}_{nU}^\intercal \widehat{\boldsymbol{N}} \boldsymbol{\mathcal{B}}_{nU} & 0 \\ 0 & 0 \end{bmatrix} d\Omega,$$

where

$$\widehat{\boldsymbol{N}} = \begin{bmatrix} N_{11} & N_{12} & 0 \\ N_{12} & N_{22} & 0 \\ 0 & 0 & 0 \end{bmatrix}. \tag{45}$$

The tangent stiffness matrix contribution $\boldsymbol{K}_{t,dmg}$, related to the damage evolution in Eq.(37), is computed as

$$\boldsymbol{K}_{t,dmg} = \boldsymbol{K}_{0D} + \boldsymbol{K}_{12D}. \tag{46}$$

The terms $\boldsymbol{K}_{0D}$ and $\boldsymbol{K}_{12D}$ are more specifically related to the damage-induced evolution of the small-strains contribution $\boldsymbol{K}_0$ to the stiffness matrix and to the contribution originating from the geometric non-linearity respectively.

Regarding the first term, from Eq.(37) ones can write

$$\Delta\left(\boldsymbol{K}_0 \boldsymbol{X}\right) = \boldsymbol{K}_0 \Delta \boldsymbol{X} + \Delta \boldsymbol{K}_0 \boldsymbol{X}. \tag{47}$$

The second term of the right hand-side in Eq.(47) can be written as

$$\Delta \boldsymbol{K}_0 \boldsymbol{X} = \Delta \begin{bmatrix} \boldsymbol{K}_0^{11} & \boldsymbol{K}_0^{12} \\ \boldsymbol{K}_0^{21} & \boldsymbol{K}_0^{22} \end{bmatrix} \begin{Bmatrix} \boldsymbol{U} \\ \boldsymbol{\Theta} \end{Bmatrix}. \tag{48}$$

The detailed computation is developed only for the first term $\boldsymbol{K}_0^{11}$ of the matrix appearing in Eq.(48), being the computation of the other terms similar. One may write

$$\Delta \left(\boldsymbol{K}_0^{11} \right) \boldsymbol{U} = \Delta \left[\int_\Omega \left(\boldsymbol{\mathcal{B}}_{pU}^\intercal \boldsymbol{A} \boldsymbol{\mathcal{B}}_{pU} + \boldsymbol{\mathcal{B}}_{nU}^\intercal \boldsymbol{A}_s \boldsymbol{\mathcal{B}}_{nU} \right) d\Omega \right] \boldsymbol{U} \tag{49}$$

and then, noting that, in the present formulation, the second term within the integral sign does not depend on damage, recalling Eq.(20)

$$\begin{aligned} \Delta \left(\boldsymbol{K}_0^{11} \right) \boldsymbol{U} &= \int_\Omega \sum_{i,k} \int_{h_{k-1}}^{h_k} \boldsymbol{\mathcal{B}}_{pU}^\intercal \Delta \left(\boldsymbol{Q}_{p,i} \right) \boldsymbol{\mathcal{B}}_{pU} \boldsymbol{U} dx_3 d\Omega = \\ &= \int_\Omega \sum_{i,k} \int_{h_{k-1}}^{h_k} \boldsymbol{\mathcal{B}}_{pU}^\intercal \frac{\partial \boldsymbol{Q}_{p,i}}{\partial \omega_i^v} \frac{\partial \omega_i^v}{\partial \omega_i} \frac{\partial \omega_i}{\partial e_{i,eq}} \frac{\partial e_{i,eq}}{\partial \boldsymbol{e}_p} \frac{\partial \boldsymbol{e}_p}{\partial \boldsymbol{X}} \Delta \boldsymbol{X} \boldsymbol{\mathcal{B}}_{pU} \boldsymbol{U} dx_3 d\Omega \end{aligned} \tag{50}$$

where the derivation chain rule has been applied and the summation is intended for $i \in \{ft, fc, mt, mc\}$ and $k \in [1, N_{ply}]$. The derivatives involved in Eq.(50) may be computed as

$$\begin{aligned} &\frac{\partial \omega_i^v}{\partial \omega_i} = \frac{\Delta \tau}{\beta + \Delta \tau}, \qquad \frac{\partial \omega_i}{\partial e_{i,eq}} = \frac{\alpha_i}{\alpha_i - 1} \left(\frac{e_{i,eq}^0}{e_{i,eq}^2} \right), \\ &\frac{\partial e_{i,eq}}{\partial \boldsymbol{e}_p} = \left\{ \frac{\partial e_{i,eq}}{\partial e_{11}} \quad \frac{\partial e_{i,eq}}{\partial e_{22}} \quad \frac{\partial e_{i,eq}}{\partial e_{12}}, \right\} \\ &\frac{\partial \boldsymbol{e}_p}{\partial \boldsymbol{X}} \Delta \boldsymbol{X} = \boldsymbol{\mathcal{B}}_{pU} \Delta \boldsymbol{U} + x_3 \boldsymbol{\mathcal{B}}_{p\Theta} \Delta \boldsymbol{\Theta} + \boldsymbol{\mathcal{B}}_{nlU} \Delta \boldsymbol{U}. \end{aligned} \tag{51}$$

Noting that the product of Eqs.(51) results in a scalar, this block is conveniently moved at

the end of the integral as follows

$$\begin{aligned}
&\int_\Omega \sum_{i,k} \int_{h_{k-1}}^{h_k} \boldsymbol{\mathcal{B}}_{pU}^\intercal \frac{\partial \boldsymbol{Q}_{p,i}}{\partial \omega_i^v} \boldsymbol{\mathcal{B}}_{pU} \boldsymbol{U} \frac{\partial \omega_i^v}{\partial \omega_i} \frac{\partial \omega_i}{\partial e_{i,eq}} \frac{\partial e_{i,eq}}{\partial \boldsymbol{e}_p} \frac{\partial \boldsymbol{e}_p}{\partial \boldsymbol{X}} \Delta \boldsymbol{X} dx_3 d\Omega = \\
&= \int_\Omega \boldsymbol{\mathcal{B}}_{pU}^\intercal \left[\sum_{i,k} \int_{h_{k-1}}^{h_k} \frac{\partial \boldsymbol{Q}_{p,i}}{\partial \omega_i^i} \boldsymbol{\mathcal{B}}_{pU} \boldsymbol{U} \zeta(\alpha_i, \beta, \Delta\tau) dx_3 \right] \boldsymbol{\mathcal{B}}_{pU} \Delta \boldsymbol{U} + \\
&+ \boldsymbol{\mathcal{B}}_{pU}^\intercal \left[\sum_{i,k} \int_{h_{k-1}}^{h_k} \frac{\partial \boldsymbol{Q}_{p,i}}{\partial \omega_i^i} \boldsymbol{\mathcal{B}}_{pU} \boldsymbol{U} \zeta(\alpha_i, \beta, \Delta\tau) x_3 dx_3 \right] \boldsymbol{\mathcal{B}}_{pU} \Delta \boldsymbol{\Theta} + \\
&+ \boldsymbol{\mathcal{B}}_{pU}^\intercal \left[\sum_{i,k} \int_{h_{k-1}}^{h_k} \frac{\partial \boldsymbol{Q}_{p,i}}{\partial \omega_i^i} \boldsymbol{\mathcal{B}}_{pU} \boldsymbol{U} \zeta(\alpha_i, \beta, \Delta\tau) dx_3 \right] \boldsymbol{\mathcal{B}}_{nlU} \Delta \boldsymbol{U} d\Omega = \\
&= \int_\Omega \boldsymbol{\mathcal{B}}_{pU}^\intercal \boldsymbol{A}^{*,1} \boldsymbol{\mathcal{B}}_{pU} \Delta \boldsymbol{U} + \boldsymbol{\mathcal{B}}_{pU}^\intercal \boldsymbol{B}^{*,1} \boldsymbol{\mathcal{B}}_{pU} \Delta \boldsymbol{\Theta} + \boldsymbol{\mathcal{B}}_{pU}^\intercal \boldsymbol{A}^{*,1} \boldsymbol{\mathcal{B}}_{nlU} \Delta \boldsymbol{U} d\Omega,
\end{aligned} \tag{52}$$

where

$$\zeta(\alpha_i, \beta, \Delta\tau) = \frac{\Delta\tau}{\beta + \Delta\tau} \frac{\alpha_i}{\alpha_i - 1} \left(\frac{e_{i,eq}^0}{e_{i,eq}^2} \right) \frac{\partial e_{i,eq}}{\partial \boldsymbol{e}_p}. \tag{53}$$

Repeating the same procedures for all the elements of the matrix $\boldsymbol{K}_0$, the final expression of the matrix $\boldsymbol{K}_{0D}$ is obtained as

$$\boldsymbol{K}_{0D} = \boldsymbol{K}_0 + \int_\Omega \begin{bmatrix} \boldsymbol{\mathcal{B}}_{pU}^\intercal \boldsymbol{A}^* \left(\boldsymbol{\mathcal{B}}_{pU} + \boldsymbol{\mathcal{B}}_{nlU} \right) & \boldsymbol{\mathcal{B}}_{pU}^\intercal \boldsymbol{B}^* \boldsymbol{\mathcal{B}}_{p\Theta} \\ \boldsymbol{\mathcal{B}}_{p\Theta}^\intercal \boldsymbol{B}^* \left(\boldsymbol{\mathcal{B}}_{pU} + \boldsymbol{\mathcal{B}}_{nlU} \right) & \boldsymbol{\mathcal{B}}_{p\Theta}^\intercal \boldsymbol{D}^* \boldsymbol{\mathcal{B}}_{p\Theta} \end{bmatrix} d\Omega, \tag{54}$$

where

$$\begin{aligned}
\boldsymbol{A}^* &= \sum_{i,k} \int_{h_{k-1}}^{h_k} \frac{\partial \boldsymbol{Q}_{p,i}}{\partial \omega_i^i} \left(\boldsymbol{\mathcal{B}}_{pU} \boldsymbol{U} + x_3 \boldsymbol{\mathcal{B}}_{p\Theta} \boldsymbol{\Theta} \right) \zeta(\alpha_i, \beta, \Delta\tau) dx_3, \\
\boldsymbol{B}^* &= \sum_{i,k} \int_{h_{k-1}}^{h_k} \frac{\partial \boldsymbol{Q}_{p,i}}{\partial \omega_i^i} \left(\boldsymbol{\mathcal{B}}_{pU} \boldsymbol{U} + x_3 \boldsymbol{\mathcal{B}}_{p\Theta} \boldsymbol{\Theta} \right) \zeta(\alpha_i, \beta, \Delta\tau) x_3 dx_3, \\
\boldsymbol{D}^* &= \sum_{i,k} \int_{h_{k-1}}^{h_k} \frac{\partial \boldsymbol{Q}_{p,i}}{\partial \omega_i^i} \left(\boldsymbol{\mathcal{B}}_{pU} \boldsymbol{U} + x_3 \boldsymbol{\mathcal{B}}_{p\Theta} \boldsymbol{\Theta} \right) \zeta(\alpha_i, \beta, \Delta\tau) x_3^2 dx_3.
\end{aligned} \tag{55}$$

The same procedure is repeated for computing the tangent stiffness terms related to the

material degradation in the non-linear geometry matrix contributions, which leads to

$$\boldsymbol{K}_{12D} = \boldsymbol{K}_{1D} + \boldsymbol{K}_{2D} \tag{56}$$

where $\boldsymbol{K}_{1D}$ is given by

$$\int_{\Omega} \begin{bmatrix} \boldsymbol{\mathcal{B}}_{pU}^{\intercal} \boldsymbol{A}^{**} \left(\boldsymbol{\mathcal{B}}_{pU} + \boldsymbol{\mathcal{B}}_{nlU}\right) + \boldsymbol{\mathcal{B}}_{nlU}^{\intercal} \boldsymbol{A}^{\#} \boldsymbol{\mathcal{B}}_{pU} & \left(\boldsymbol{\mathcal{B}}_{pU}^{\intercal} \boldsymbol{B}^{**} \boldsymbol{\mathcal{B}}_{p\Theta} + \boldsymbol{\mathcal{B}}_{nlU}^{\intercal} \boldsymbol{B}^{\#} \boldsymbol{\mathcal{B}}_{p\Theta}\right) \\ \left(\boldsymbol{\mathcal{B}}_{p\Theta}^{\intercal} \boldsymbol{B}^{**} \boldsymbol{\mathcal{B}}_{pU} + \boldsymbol{\mathcal{B}}_{p\Theta}^{\intercal} \boldsymbol{B}^{**} \boldsymbol{\mathcal{B}}_{nlU}\right) & \boldsymbol{\mathcal{B}}_{p\Theta}^{\intercal} \boldsymbol{D}^{**} \boldsymbol{\mathcal{B}}_{p\Theta} \end{bmatrix} d\Omega \tag{57}$$

and

$$\boldsymbol{K}_{2D} = \int_{\Omega} \begin{bmatrix} \boldsymbol{\mathcal{B}}_{nlU}^{\intercal} \boldsymbol{A}^{\#} \boldsymbol{\mathcal{B}}_{nlU} & 0 \\ 0 & 0 \end{bmatrix} d\Omega, \tag{58}$$

in which

$$\begin{aligned} \boldsymbol{A}^{**} &= \sum_{i,k} \int_{h_{k-1}}^{h_k} \frac{1}{2} \frac{\partial \boldsymbol{Q}_{p,i}}{\partial \omega_i^i} \boldsymbol{\mathcal{B}}_{nlU} \boldsymbol{U} \zeta(\alpha_i, \beta, \Delta\tau) dx_3 \\ \boldsymbol{B}^{**} &= \sum_{i,k} \int_{h_{k-1}}^{h_k} \frac{1}{2} \frac{\partial \boldsymbol{Q}_{p,i}}{\partial \omega_i^i} \boldsymbol{\mathcal{B}}_{nlU} \boldsymbol{U} \zeta(\alpha_i, \beta, \Delta\tau) x_3 dx_3 \\ \boldsymbol{D}^{**} &= \sum_{i,k} \int_{h_{k-1}}^{h_k} \frac{1}{2} \frac{\partial \boldsymbol{Q}_{p,i}}{\partial \omega_i^i} \boldsymbol{\mathcal{B}}_{nlU} \boldsymbol{U} \zeta(\alpha_i, \beta, \Delta\tau) x_3^2 dx_3 \\ \boldsymbol{A}^{\#} &= \sum_{i,k} \int_{h_{k-1}}^{h_k} \frac{\partial \boldsymbol{Q}_{p,i}}{\partial \omega_i^i} \left(\boldsymbol{\mathcal{B}}_{pU} \boldsymbol{U} + x_3 \boldsymbol{\mathcal{B}}_{p\Theta} \boldsymbol{\Theta} + \frac{1}{2} \boldsymbol{\mathcal{B}}_{nlU} \boldsymbol{U}\right) \zeta(\alpha_i, \beta, \Delta\tau) dx_3 \\ \boldsymbol{B}^{\#} &= \sum_{i,k} \int_{h_{k-1}}^{h_k} \frac{\partial \boldsymbol{Q}_{p,i}}{\partial \omega_i^i} \left(\boldsymbol{\mathcal{B}}_{pU} \boldsymbol{U} + x_3 \boldsymbol{\mathcal{B}}_{p\Theta} \boldsymbol{\Theta} + \frac{1}{2} \boldsymbol{\mathcal{B}}_{nlU} \boldsymbol{U}\right) \zeta(\alpha_i, \beta, \Delta\tau) x_3 dx_3. \end{aligned} \tag{59}$$